

Interpretation of the in-plane infrared response of the high- T_c cuprate superconductors involving spin fluctuations revisited

Petr Cásek¹, Christian Bernhard², Josef Humlíček¹, and Dominik Munzar^{1*}

¹*Institute of Condensed Matter Physics, Faculty of Science,
Masaryk University, Kotlářská 2, 61137 Brno, Czech Republic*

²*Max-Planck-Institut für Festkörperforschung, Heisenbergstrasse 1, D-70569 Stuttgart, Germany*

The in-plane infrared response of the high- T_c cuprate superconductors was studied using the spin-fermion model, where charged quasiparticles of the copper-oxygen planes are coupled to spin fluctuations. First, we analyzed structures of the superconducting-state conductivity reflecting the coupling of the quasiparticles to the resonance mode observed by neutron scattering. The conductivity σ computed with the input spin susceptibility in the simple form of the mode exhibits two prominent features: an onset of the real part of σ starting around the frequency ω_0 of the mode and a maximum of a related function $W(\omega)$, roughly proportional to the second derivative of the scattering rate $[1/\tau](\omega)$, centered approximately at $\omega = \omega_0 + \Delta_0/\hbar$, where Δ_0 is the maximum value of the superconducting gap. The two structures are well known from earlier studies. Their physical meaning, however, has not been sufficiently elucidated thus far. Our analysis involving quasiparticle spectral functions provides a clear interpretation. Second, we explored the role played by the spin-fluctuation continuum, whose spectral weight is known to be much larger than the one of the mode. We have shown that the experimental spectra of $1/\tau$ can be approximately reproduced by augmenting the resonant-mode component of the spin susceptibility by a suitable continuum component with a considerably higher spectral weight and with a characteristic width of several hundreds meV. The computed spectra of $1/\tau$ display a new structure in the mid-infrared which is related to the finite width of the occupied part of the conduction band. Third, we investigated the temperature dependence (TD) of σ assuming that the normal state spin susceptibility consists of an overdamped low energy mode and the continuum component. The differences between the experimental normal-state spectra and those of the superconducting state, including some interesting effects at higher frequencies, are reasonably well reproduced. Motivated by recent experimental (ellipsometric) works by Molegraaf and coworkers [H. J. A. Molegraaf *et al.*, *Science* **295**, 2239 (2002).] and Boris and coworkers [A. V. Boris *et al.*, *Science* **304**, 708 (2004).], we further studied the TDs of the effective kinetic energy K.E. and of the intraband spectral weight I_O . Calculations for the trivial case of noninteracting quasiparticles in the normal state and a BCS-like superconducting state reveal a strong sensitivity of the TD of I_O to details of the dispersion relation. The TDs of K.E. and I_O in the interacting case, for the set of the values of the input parameters used throughout this work, are similar to those of the trivial case. The physics beyond the changes occurring when going from the normal to the superconducting state, however, is shown to be more complex, involving, besides the formation of the gap, also a feedback effect of the spin fluctuations on the quasiparticles and a significant shift of the chemical potential.

I. INTRODUCTION

Models of the electronic structure of the high- T_c cuprate superconductors (HTCS), where charged quasiparticles of the copper-oxygen planes are coupled to spin fluctuations (SF) (for review see Refs. 1,2) possess two appealing features. (a) They provide a straightforward explanation of the symmetry of the order parameter and (b) the same value of the coupling constant leads both to a fairly good agreement between theory and experiment for the normal state and to values of T_c of 50 – 100 K.

On the other hand, these models suffer two important deficiencies. (a) They cannot be rigorously derived starting from a well established microscopic hamiltonian such as the hamiltonian of the 2D one-band Hubbard model. They can only be motivated by some perturbation expansions of the latter. Within the so called conserving fluctuation exchange (FLEX) approximation^{3,4,5,6,7,8,9}, e.g., an important term in the expression for the quasiparticle

selfenergy $\Sigma(\mathbf{k}, i\omega_n)$ reads

$$\frac{1}{\beta N} \frac{3U^2}{2} \sum_{\mathbf{q}, i\Omega_m} \chi_{RPA}(\mathbf{q}, i\Omega_m) G(\mathbf{k} - \mathbf{q}, i\omega_n - i\Omega_m), \quad (1)$$

where $i\omega_n$ ($i\Omega_m$) are the fermion (boson) Matsubara frequencies, $\beta = 1/(k_B T)$, N is the number of momentum points, and U is the Hubbard parameter. Further, G is the dressed quasiparticle propagator and χ_{RPA} the random-phase-approximation(RPA)-based expression for the spin susceptibility. The expression for the selfenergy used within the SF-based models has precisely the same structure:

$$\frac{1}{\beta N} \frac{3g^2}{4} \sum_{\mathbf{q}, i\Omega_m} \chi_{SF}(\mathbf{q}, i\Omega_m) G(\mathbf{k} - \mathbf{q}, i\omega_n - i\Omega_m), \quad (2)$$

where g and χ_{SF} are the model coupling constant and spin susceptibility, respectively. This can be considered as a kind of formal justification of the SF-based approaches. A typical value of g of 0.5 eV, however, is

an order of magnitude lower than that of U resulting from first-principles calculations of $5 - 10$ eV^{10,11}. (b) The second problem of the SF-based models concerns the choice of the function χ_{SF} . In the spirit of the models, χ_{SF} should match the true spin susceptibility χ accessible to experimental investigations. Unfortunately, the available experimental data are not yet sufficient to determine χ in the relevant spectral range. This applies especially to the normal state (NS) of optimum doped and overdoped materials, where the spin fluctuations are relatively weak. The form of χ_{SF} has thus to be guessed, at least to some extent. In the classical series of papers, Monthoux *et al.*^{12,13,14} have adopted the Millis-Monien-Pines formula¹⁵:

$$\chi_{MMP}(\mathbf{q}, \omega) = \frac{\chi_Q}{1 + (\mathbf{q} - \mathbf{Q})^2 \xi^2 - i\omega/\omega_{sf}}, \quad (3)$$

where $\mathbf{Q} = (\pi/a, \pi/a)$ is the antiferromagnetic wave vector, a is the in-plane lattice parameter, ξ the antiferromagnetic coherence length, and ω_{sf} is the parameter that specifies the frequency of the relaxation mode (at a fixed \mathbf{q} , $\chi''_{MMP}(\mathbf{q}, \omega)$ exhibits a broad maximum centered at $\omega = \omega_{sf}[1 + (\mathbf{q} - \mathbf{Q})^2 \xi^2]$, i.e., a relaxation mode).

The situation is simpler for the superconducting state (SCS), where a sharp resonance in χ (“magnetic mode”) centered at $\mathbf{q} = \mathbf{Q}$, $\mathbf{Q} = (\pi/a, \pi/a)$, and $\omega = \omega_0$, $\omega_0 \approx 40$ meV, has been detected in neutron scattering experiments (see Refs. 16,17, 18,19 and references therein). For some compounds the shape of the resonance is well known and it is thus possible to investigate the coupling between the mode and the charge carriers without any *ad hoc* assumptions regarding the form of χ_{SF} . Let us emphasize that there must be a coupling between the well defined mode and the well defined Bogoliubov quasiparticles and it should be considered in any theory of superconductivity in the HTCS, in particular, when describing single-particle excitations (observed by photoemission) and two-particle excitations (observed, among others, by optics). Such considerations may help to clarify the role played by the SF in the mechanism of superconductivity. The single-particle case has been reviewed in detail in Refs. 1 and 20. An important observation is that the peak-dip-hump structure observed in superconducting-state angle-resolved-photoemission spectra (for review see Ref. 21) at and around $(\pi/a, 0)$ can be understood and described in terms of the above mentioned coupling. This result, together with several other findings, suggests that the SF are an important player in the mechanism. In this work we focus on the influence of the coupling on the in-plane infrared response of the HTCS in the superconducting state.

The SF-based approach has been pioneered in this context by Schachinger, Carbotte, and Marsiglio²² and by Quinlan, Hirschfeld, and Scalapino²³. The former group used the boson spectral density proportional to $\chi''_{MMP}(\mathbf{q} = \mathbf{Q}, \omega)$, in the work of the latter χ_{RPA} has been used. The real part of the in-plane infrared conductivity, $\sigma_1(\omega)$, resulting from these computations ex-

hibits the following trends: (i) Below T_c and for frequencies lower than $\sim 4\Delta_0$, where Δ_0 is the maximum value of the superconducting gap, it decreases with decreasing temperature. (ii) It does not possess a true energy gap, even at very low temperatures and in the absence of any impurity scattering. Instead, at low temperatures, it increases gradually with increasing ω . (iii) The increase becomes steeper above the characteristic spin-fluctuation frequency of $\omega_{sf} = 30$ meV²² or $\Delta_0 - 2\Delta_0$ ²³. (iv) A very broad maximum appears in the low-temperature spectra around $\sim 4\Delta_0$. These findings are roughly consistent with experimental data^{24,25,26,27,28,29}, except for two features. First, the data contain additional sharp structures at low frequencies. These are probably related to charge inhomogeneities and will not be discussed here. Second, the increase of $\sigma_1(\omega)$ in the data appears to be less gradual than in the theoretical spectra. The data rather seem to exhibit an onset starting around $300 - 400$ cm⁻¹. This may be related to the presence of a sharp feature in the spin-fluctuation spectra below T_c , i.e., to the magnetic mode, which has not been considered in Refs. 22 and 23.

The mode has been taken into account by two of the authors and M. Cardona (MBC)³⁰, who employed a form of χ_{SF} reflecting the results of the neutron scattering experiments:

$$\chi_{RM}(\mathbf{q}, \omega) = \frac{1}{1 + (\mathbf{q} - \mathbf{Q})^2 \xi^2} \frac{F}{\omega_0^2 - \omega^2 - i\Gamma\omega}, \quad (4)$$

where Γ is the broadening of the resonance mode and F expresses its “oscillator strength”. This study provided a tentative interpretation of the onset feature: the final states consist, in the first approximation, of two Bogoliubov quasiparticles and the magnetic mode; the minimum excitation energy is thus $\hbar\omega_0 \approx 40$ meV ≈ 320 cm⁻¹ and the broad maximum around 1000 cm⁻¹ corresponds to excitations involving quasiparticles around the saddle point and the mode. Carbotte, Schachinger, and Basov (CSB)³¹ also interpreted the data in terms of the magnetic mode but an inverse strategy has been used. Their approach is based on a relation between the conductivity and the electron-phonon spectral density $\alpha^2 F(\omega)$ that applies to the normal state of a weakly coupled isotropic electron-phonon system³².

$$\alpha^2 F(\omega) \approx W(\omega) = \frac{\varepsilon_0 \omega_{pl}^2}{2\pi} \frac{d^2}{d\omega^2} \left[\omega \operatorname{Re} \frac{1}{\sigma(\omega)} \right], \quad (5)$$

where ω_{pl} is the plasma frequency of the free charge carriers. CSB assumed (and to some extent verified by computing $\sigma(\omega)$ within Eliashberg formalism) that a slightly modified equation,

$$I^2 \chi_{ef}(\omega - \Delta_{max}) \approx W(\omega) = \frac{\varepsilon_0 \omega_{pl}^2}{2\pi} \frac{d^2}{d\omega^2} \left[\omega \operatorname{Re} \frac{1}{\sigma(\omega)} \right], \quad (6)$$

can be used to obtain the “effective electron-spin-fluctuation spectral function” $I^2 \chi_{ef}(\omega)$ of a *d*-wave superconductor²². The main point of CSB is that $\chi_{ef}(\omega)$,

as determined from the optical data, contains a sharp structure that is fairly similar to the one of $\chi''(\mathbf{Q}, \omega)$, i.e., to the neutron resonance. Based on this finding, CSB concluded that the infrared data reflect a coupling of the charge carriers to the magnetic mode. The coupling strength inferred from experiment is found to be sufficient to account for the high value of T_c . The relation between $\sigma_1(\omega)$ and the magnetic mode has been further explored by Abanov, Chubukov, and Schmalian (ACS)^{33,34}. For example, they predicted a sharp onset of $\sigma_1(\omega)$ located at $\hbar\omega = 2\Delta_0 + \hbar\omega_0$ (see Fig. 2 of Ref. 33). The three approaches (MBC, CSB, ACS) differ in their emphasis and computational formalism. MBC showed that the superconducting-state infrared data can be understood in terms of the SF-based model with the spin susceptibility in the form of the neutron peak and focused on the onset in the conductivity spectra starting, according to the model, around ω_0 . CSB found an approximate solution of the inverse problem, the spectral function $W(\omega)$, and attributed its main maximum to the magnetic mode shifted by Δ_0 towards higher frequencies. Finally, ACS concentrated on the contribution to the conductivity of the so called hot spots, i.e., intercepts of the Fermi surface and the antiferromagnetic-Brillouin-zone (BZ) boundary, and they argued that this contribution is the dominant one. Regarding the formalism, all the three groups expressed the quasiparticle selfenergy using the SCS version of Eq. 2 and the conductivity using the textbook formulas³⁵, where the vertex corrections are neglected. The differences consist in treating the propagator G and the susceptibility χ_{SF} . In the work of MCB, G is replaced with the bare Nambu matrix containing an estimated superconducting gap of $d_{x^2-y^2}$ symmetry, i.e., with the BCS expression. The approach is thus not self-consistent. On the other hand, it has two important advantages, not shared by the other two approaches, besides its formal simplicity: (a) It is not restricted to models, where the SF are the only cause of superconductivity. (b) The full q -dependence of χ is taken into account. The same approach has been used in the studies of the single-particle properties by Eschrig and Norman and coworkers (see Ref. 20 and references therein) and, in the context of electron-phonon interaction, by Sandvik, Scalapino, and Bickers³⁶. CSB obtain the propagator G by solving Eliashberg equations with a separable interaction, i.e., in a selfconsistent way. ACS use an approximate form of these equations valid in a region around the hot spots. Not only the propagator but also the spin susceptibility is treated in a self-consistent way.

The structures in the conductivity spectra can be relatively easily related to and understood in terms of those of the quasiparticle spectral functions (in the absence of vertex corrections). Such an analysis, however, has not yet been performed, except for some observations regarding the contributions of the hot spots^{30,34} and the optical scattering rate³⁷. One of the aims of the present paper is to provide a detailed interpretation of the onset starting around ω_0 discussed by MBC and of the main maximum

of the function $W(\omega)$ emphasized by CSB in terms of the quasiparticle spectral function. Among others, we explore the role played by the hot spots.

The structure of the paper is the following. In Sec. II we summarize the basic equations of our approach and in Sec. III we discuss the input parameters and present some computational details. Section IV contains our results. We start with the quasiparticle spectral functions, that are compared with those computed by Eschrig and Norman²⁰ (Subsec. IV A), and contributions of the individual \mathbf{k} -points to the real part of the conductivity (Subsec. IV B). Subsecs. IV C and IV D deal with the spectra of the total conductivity, in particular with its onset around ω_0 , and with the structures of the scattering rate and the function $W(\omega)$, respectively. In Subsec. IV E we comment on the role of the SF continuum. Some aspects of the temperature dependence (TD) of the spectra, as the role of the TD of χ_{SF} , and the TD of the integrated spectral weight, that has been recently related to changes of the effective in-plane kinetic energy^{29,38}, are addressed in Subsec. IV F. A summary and our conclusions are presented in Sec. V. Readers who are interested only in the main findings of the paper can skip Secs. II and III and some more technical parts of Sec. IV.

II. THEORETICAL FRAMEWORK

Our starting point is the Hamiltonian of the spin-fermion model:

$$H = H_0 + H_{\text{int}}, \quad (7)$$

where

$$H_0 = \sum_{\mathbf{k}\alpha} \epsilon_{\mathbf{k}} c_{\mathbf{k}\alpha}^+ c_{\mathbf{k}\alpha}, \quad (8)$$

$$H_{\text{int}} = g \sum_{\mathbf{q}} \mathbf{s}(\mathbf{q}) \cdot \mathbf{S}(-\mathbf{q}). \quad (9)$$

Here $\epsilon_{\mathbf{k}}$ is the quasiparticle dispersion, α is the spin index, g is the spin-fermion coupling constant,

$$\mathbf{s}(\mathbf{q}) = \frac{1}{\sqrt{N}} \frac{1}{2} \sum_{\mathbf{k}\alpha\beta} c_{\mathbf{k}+\mathbf{q}\alpha}^+ \tau_{\alpha\beta} c_{\mathbf{k}\beta} \quad (10)$$

is the Fourier component of the electronic spin, $\tau = (\tau_1, \tau_2, \tau_3)$ is the vector of the Pauli matrices, and $\mathbf{S}(\mathbf{q})$ the spin-fluctuation operator. The latter quantity is defined so that its retarded Green's function is equal to the negatively taken spin susceptibility,

$$\chi_{ij}(\mathbf{q}, \omega) = \frac{1}{\hbar} \int_{-\infty}^{\infty} \chi_{ij}(\mathbf{q}, t) e^{i\omega t} dt \quad (11)$$

with

$$\chi_{ij}(\mathbf{q}, t) = i\Theta(t) \langle [s_i(\mathbf{q}, t), s_j(-\mathbf{q}, 0)] \rangle. \quad (12)$$

It is assumed that $\chi_{ij}(\mathbf{q}, \omega)$ is isotropic, i.e., $\chi_{ij}(\mathbf{q}, \omega) = \delta_{ij} \chi(\mathbf{q}, \omega)$.

A. Quasiparticle selfenergy and spectral function

We follow here the approach of Ref. 30 and express the quasiparticle selfenergy $\Sigma(\mathbf{k}, iE_n)$ using second order perturbation theory (H_{int} being the perturbation) and starting from a BCS state with an estimated superconducting gap of $d_{x^2-y^2}$ symmetry. The resulting formula for $\Sigma(\mathbf{k}, iE_n)$ (2 by 2 matrix) represents a SCS version of Eq. 2:

$$\begin{aligned} \Sigma(\mathbf{k}, iE_n) &= \\ &= \frac{1}{\beta N} \frac{3g^2}{4} \sum_{\mathbf{q}} \sum_{i\Omega_m} \chi_{SF}(\mathbf{q}, i\Omega_m) G_0(\mathbf{k} - \mathbf{q}, iE_n - i\hbar\Omega_m) \end{aligned} \quad (13)$$

with

$$G_0(\mathbf{k}, iE_n) = \frac{iE_n\tau_0 + (\epsilon_{\mathbf{k}} - \mu)\tau_3 + \Delta_{\mathbf{k}}\tau_1}{(iE_n)^2 - (\epsilon_{\mathbf{k}} - \mu)^2 - \Delta_{\mathbf{k}}^2}. \quad (14)$$

Here G_0 is the bare Nambu Green's function iE_n are the fermion Matsubara energies ($iE_n = i\hbar\omega_n$), μ is the chemical potential, and $\Delta_{\mathbf{k}}$ the superconducting gap. The full Nambu propagator G is given by the Dyson equation, $G^{-1} = G_0^{-1} - \Sigma^{-1}$, and the matrix spectral function $A(\mathbf{k}, E) = -2 \text{Im} [G_{ret}(\mathbf{k}, E)]$ by

$$A(\mathbf{k}, E) = -2 \text{Im} [G_0^{-1}(\mathbf{k}, iE_n) - \Sigma(\mathbf{k}, iE_n)]_{iE_n \rightarrow E + i\delta}^{-1}. \quad (15)$$

Equation 13 can be further rewritten into a form which is more suitable for practical computations:

$$\Sigma(\mathbf{k}, iE_n) = \frac{1}{N} \frac{3g^2}{4} \sum_{\mathbf{q}} \int_0^\infty d\omega \hbar B(\mathbf{q}, \omega) \left\{ \frac{1}{2}(T_+ + T_-)\tau_0 + \frac{\epsilon_{\mathbf{k}+\mathbf{q}}}{2E_{\mathbf{k}+\mathbf{q}}}(T_+ - T_-)\tau_3 + \frac{\Delta_{\mathbf{k}+\mathbf{q}}}{2E_{\mathbf{k}+\mathbf{q}}}(T_+ - T_-)\tau_1 \right\}, \quad (16)$$

where

$$T_{\pm} = \frac{N_B(\hbar\omega) + n_F(\pm E_{\mathbf{k}+\mathbf{q}})}{iE_n + \hbar\omega \mp E_{\mathbf{k}+\mathbf{q}}} + \frac{N_B(\hbar\omega) + 1 - n_F(\pm E_{\mathbf{k}+\mathbf{q}})}{iE_n - \hbar\omega \mp E_{\mathbf{k}+\mathbf{q}}}. \quad (17)$$

In the preceding equations

$$B(\mathbf{q}, \omega) = \frac{1}{\pi} \text{Im} \{ \chi_{SF}(\mathbf{q}, \omega) \} \quad (18)$$

is the spectral function of the spin fluctuations. The quasiparticle excitation energies $E_{\mathbf{k}}$ are defined as usual: $E_{\mathbf{k}} = \sqrt{(\epsilon_{\mathbf{k}} - \mu)^2 + \Delta_{\mathbf{k}}^2}$, N_B and n_F are the Bose-Einstein and Fermi-Dirac distribution functions, respectively. For a single CuO₂ plane ($1/N$) $\sum_{\mathbf{q}}$ in Eqs. 13, 16 can be replaced with $\int_{2D \text{ BZ}} d^2\mathbf{q}/(2\pi)^2$.

B. Optical response

The Kubo formula for the conductivity $\sigma_{ij}(\mathbf{q}, \omega)$ ($i, j \in \{x, y, z\}$) reads³⁹:

$$\sigma_{ij}(\mathbf{q}, \omega) = \frac{i}{\omega + i\delta} \left[R_{ij}(\mathbf{q}, \omega) + \frac{n_0 e^2}{m} \delta_{ij} \right], \quad (19)$$

where

$$R_{ij}(\mathbf{q}, \omega) = -\frac{i}{\hbar} \int_{-\infty}^{\infty} dt \theta(t) e^{i\omega t} \langle [j_i(\mathbf{q}, t), j_j(-\mathbf{q}, 0)] \rangle \quad (20)$$

is the retarded correlation function of the paramagnetic current density operator and n_0 is the average electron

density. The two terms in the bracket on the right hand side of Eq. 19 [multiplied by the factor $i/(\omega + i\delta)$] are the paramagnetic and the diamagnetic term, respectively. The contribution to $\sigma_{ij}(\mathbf{q}, \omega)$ of charge carriers in a single band is given by a formula⁴⁰ which has the same structure as Eq. 19. The Fourier component of the corresponding current density operator is given by

$$\mathbf{j}(\mathbf{q}) = \frac{e}{\sqrt{V}} \sum_{\mathbf{k}\alpha} \mathbf{v} \left(\mathbf{k} + \frac{\mathbf{q}}{2} \right) c_{\mathbf{k}\alpha}^+ c_{\mathbf{k}+\mathbf{q}\alpha}, \quad (21)$$

where $\mathbf{v}(\mathbf{k}) = (1/\hbar) \partial\epsilon/\partial\mathbf{k}$, and the diamagnetic term is replaced with

$$-\frac{i}{\omega + i\delta} \frac{e^2}{\hbar^2} \langle K_{ij} \rangle, \quad K_{ij} = -\frac{1}{V} \sum_{\mathbf{k}\alpha} \frac{\partial^2 \epsilon}{\partial k_i \partial k_j} c_{\mathbf{k}\alpha}^+ c_{\mathbf{k}\alpha}. \quad (22)$$

For easy reference, we summarize here some basic properties of the optical conductivity $\sigma_{ij}(\omega) = \sigma_{ij}(\mathbf{q} = 0, \omega)$. It consists of a singular part $\sigma_{ij}^s(\omega)$, related to the condensate, and a regular part $\sigma_{ij}^r(\omega)$. They are given by

$$\sigma^s(\omega) = \frac{i\varepsilon_0 \omega_{\text{pl,sc}}^2}{\omega + i\delta} \quad (23)$$

and

$$\sigma^r(\omega) = \frac{i}{\omega} [R(\omega) - \text{Re}\{R(0)\}]. \quad (24)$$

The tensor indices are omitted for simplicity, $\omega_{\text{pl,sc}}$ is the plasma frequency of the superfluid,

$$\omega_{\text{pl,sc}}^2 = -\frac{1}{\varepsilon_0} \left[\frac{e^2}{\hbar^2} \langle K \rangle - \text{Re}\{R(0)\} \right] \quad (25)$$

and $R(\omega) = R(\mathbf{q} = 0, \omega)$. The imaginary part $\sigma_2(\omega)$ of $\sigma(\omega)$ can be expressed in terms of the real part, $\sigma_1(\omega)$, using the following Kramers-Kronig relation:

$$\sigma_2(\omega) = -\frac{1}{\omega} \frac{e^2}{\hbar^2} \langle K \rangle + \frac{2}{\omega \pi} P \int_{0^+}^{\infty} d\omega' \frac{\omega'^2 \sigma_1(\omega') - \omega^2 \sigma_1(\omega)}{\omega^2 - \omega'^2}. \quad (26)$$

The symbol 0^+ in the lower limit means that the singular component of σ_1 , $\sigma_1^s(\omega) = \pi \varepsilon_0 \omega_{\text{pl,sc}}^2 \delta(\omega)$, is excluded from the integration. The function $\sigma_1(\omega)$ (including its singular component) satisfies the following useful sum rule:

$$I_O = \int_0^{\infty} d\omega \sigma_1(\omega) = \frac{\pi}{2} \varepsilon_0 \omega_{\text{pl}}^2 = -\frac{\pi}{2} \frac{e^2}{\hbar^2} \langle K \rangle, \quad (27)$$

which allows us to express the plasma frequency of the superfluid as

$$\omega_{\text{pl,sc}}^2 = \omega_{\text{pl}}^2 - \frac{2}{\pi \varepsilon_0} \int_{0^+}^{\infty} d\omega \sigma_1(\omega). \quad (28)$$

The correlation function $R_{ij}(\omega)$, which is the key quan-

ty of the theory, can be obtained by the analytical continuation of the corresponding Matsubara Green's function $P_{ij}(\mathbf{q}, i\Omega_m)$. Using the Wick's theorem and neglecting vertex corrections we obtain⁴¹:

$$P_{ij}(\mathbf{q}, i\Omega_m) = -2e^2 \frac{1}{V} \sum_{\mathbf{k}} v_i \left(\mathbf{k} + \frac{\mathbf{q}}{2} \right) v_j \left(\mathbf{k} + \frac{\mathbf{q}}{2} \right) L(\mathbf{k}, \mathbf{q}, i\Omega_m), \quad (29)$$

where $L(\mathbf{k}, \mathbf{q}, i\Omega_m) =$

$$= -\frac{1}{2\beta} \sum_{n=-\infty}^{\infty} \text{Tr}[G(\mathbf{k} + \mathbf{q}, iE_n + i\hbar\Omega_m) G(\mathbf{k}, iE_n)]. \quad (30)$$

The regular component of $\sigma_{ij,1}(\omega)$ can be expressed in terms of the matrix spectral function of Eq. 15 as follows⁴²:

$$\sigma_{ij,1}(\omega) = \frac{e^2}{2\omega} \frac{1}{V} \sum_{\mathbf{k}} v_i(\mathbf{k}) v_j(\mathbf{k}) \int \frac{dE}{2\pi} \text{Tr}[A(\mathbf{k}, E) A(\mathbf{k}, E + \hbar\omega)] \times [n_F(E) - n_F(E + \hbar\omega)]. \quad (31)$$

For a superconductor containing N_p equivalent and weakly coupled CuO_2 planes within a unit cell, $(1/V) \sum_{\mathbf{k}}$ in Eqs. 22, 29, 31 can be replaced with $(N_p/d) \int_{2\text{D BZ}} d^2 \mathbf{k} / (2\pi)^2$, where d is the lattice parameter along the c -axis.

III. INPUT PARAMETERS AND COMPUTATIONAL DETAILS

A. Dispersion relation

In this work we use a tight-binding expansion of the in-plane dispersion relation including the second nearest neighbor hopping terms:

$$\varepsilon(\mathbf{k}) = -2t[\cos(k_x a) + \cos(k_y a)] - 4t' \cos(k_x a) \cos(k_y a). \quad (32)$$

The values of the parameters are the same as in Ref. 30 and they are summarized in Table 1. The corresponding Fermi surface is shown in part (a) of Fig. 1. For comparison, the Fermi surface, corresponding to the six-parameter fit of the dispersion relation of optimally doped $\text{Bi}_2\text{Sr}_2\text{CaCu}_2\text{O}_8$ (Bi-2212) used in Ref. 20, is shown in part (b). The figure is further used to introduce a notation of some important \mathbf{k} -points. Within the SF-based scenarios, the quasiparticles around the CS (HS) are weakly (strongly) renormalized by the spin-fermion

coupling. The CS coincides with the node of the superconducting gap whereas the HS is located in the region of high values of $|\Delta|$.

Our approach will be applied here to the bilayer compounds, i.e., materials, that contain two CuO_2 planes within a unit cell. The conduction band of these compounds can be expected to be splitted into the bonding branch and the antibonding branch⁴³. For a long time, it has not been clear, whether such splitting indeed occurs or is suppressed by strong correlations in the CuO_2 planes. Two well defined bands were recently observed in photoemission experiments on strongly overdoped Bi-2212 and some signatures of the splitting have been reported also for optimally doped and underdoped Bi-2212^{44,45,46} (for a review see Ref. 21). It has been proposed that some of the effects associated earlier with the magnetic mode, in particular the peak-dip-hump structure of the photoemission spectra, can be understood solely in terms of the two bands. Subsequently it has been shown, however, that a “true”, i.e., linked to selfenergy effects, peak-dip-hump structure develops in the spectra below T_c ^{47,48}. In the present study, the bonding-antibonding splitting is not taken into account, i.e., two identical conduction bands per unit cell are assumed, corresponding to two equivalent and independent planes. It is possible to go beyond this approximation^{8,47,49} but we believe that it would not seriously modify our conclusions regarding the in-plane

| $a(\text{\AA})$ | $d(\text{\AA})$ | t (eV) | t' (eV) | μ (eV) | Δ_0 (eV) | g (eV) | $\hbar\omega_0$ (eV) | Γ (eV) | ξ (\text{\AA}) |
|-----------------|-----------------|----------|-----------|------------|-----------------|----------|----------------------|---------------|--------------------|
| 3.828 | 11.650 | 0.250 | -0.100 | -0.350 | 0.030 | 0.350 | 0.040 | 0.010/0 | 9.0 (=2.35 a) |

TABLE 1: Values of the parameters used in the computations. The values of a and d correspond to $\text{YBa}_2\text{Cu}_3\text{O}_{7-\delta}$. We consider two CuO_2 planes within a unit cell, as in $\text{YBa}_2\text{Cu}_3\text{O}_{7-\delta}$, i.e., $N_p = 2$.

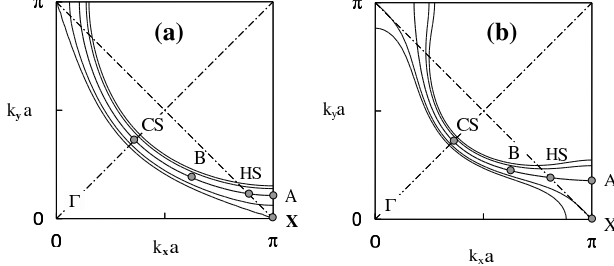


FIG. 1: Fermi surface (thick line) for the dispersion given by Eq. 32 (a) and for the dispersion of Ref. 20 (b). Supplementary contours (thin lines) correspond to excitation energies of ± 0.033 eV and ± 0.050 eV. A notation of some special points is introduced. The point CS (“cold spot”) is the crossing point of the Fermi surface and the BZ diagonal (dashed-dotted line starting in the Γ point). The point HS (“hot spot”) is the crossing point of the Fermi surface and the antiferromagnetic BZ boundary (dashed-dotted line starting in the X point). The point B is located between the CS and the HS and its (dimensionless) coordinates are (1.96, 0.60) and (1.96, 0.78) in (a) and (b), respectively.

infrared spectra.

B. Superconducting gap

If not specified in the text, we use a common ansatz for the superconducting gap of $d_{x^2-y^2}$ -symmetry:

$$\Delta(\mathbf{k}) = \frac{\Delta_0}{2} [\cos(k_x a) - \cos(k_y a)] \quad (33)$$

with $\Delta_0 = 30$ meV, a value close to the experimental result for optimally doped Bi-2212²¹. The coupling to the spin-fluctuations slightly enhances the value of the gap in the region around the HS. For the value of g of 350 meV used in our computations, the renormalized value of $|\Delta|$ exactly at the hot spot is about 35 meV. This fact, however, has no significant impact on the quantities discussed.

C. Spin susceptibility and the coupling constant

In most of the computations we use the spin susceptibility of the resonance-mode form of Eq. 4 with the values

of the input parameters given in Table 1. The FWHM of the resonance peak Γ is small as compared to both ω_0 and Δ_0 . It can be therefore neglected, in the first approximation, an approach applied by Eschrig and Norman²⁰. We have performed the calculations for both $\Gamma = 10$ meV and $\Gamma = 0$, i.e.,

$$B(\mathbf{q}, \omega) = \frac{F\pi}{1 + (\mathbf{q} - \mathbf{Q})^2 \xi^2} \delta(\omega - \omega_0), \quad (34)$$

in order to identify the role of the finite linewidth. In the following we shall refer to the calculations with $\Gamma = 10$ meV and $\Gamma = 0$ as to those with the broad and the sharp magnetic resonance, respectively. The value of the “oscillator-strength” parameter F is determined by using the same normalization condition as in Ref. 30:

$$I_M = \hbar \int \frac{a^2 d^2 q}{(2\pi)^2} \int_0^\infty d\omega (2N_B(\hbar\omega) + 1) B(\mathbf{q}, \omega) = \frac{1}{4}, \quad (35)$$

where $B(\mathbf{q}, \omega)$ is the spectral function of the spin fluctuations defined by Eq. 18. Equation 35 represents an approximate “total momentum sum rule” (see Ref. 18 for a discussion).

Note that when using χ_{SF} of the resonance-mode form together with Eq. 35 we make two approximations. (a) Within the model of two identical conduction bands per bilayer unit cell the effective spin susceptibility is equal to the average of the so called odd (χ_o) and even (χ_e) component (for a definition see Ref. 18). Here we take into account only the resonant part of χ_o , i.e., we do not consider χ_e and the continuum part of χ_o . This may be a reasonable starting point for an analysis of the low-energy phenomena. First, the magnitude of χ_o is typically by a factor of 2-3 larger than that of χ_e ^{18,50}, and second, the continuum part cannot be expected to cause any sharp structure in the quasiparticle selfenergy (see Ref. 20 for a detailed discussion). (b) In Eq. 35 the resonance is assumed to collect one half of the total magnetic spectral weight, $I_M = 1/4$. Experimentally, the value of I_M in Eq. 35 corresponding to the mode is only about $0.01 \times (1/4)$ for optimally doped $\text{YBa}_2\text{Cu}_3\text{O}_{7-\delta}$ (Y-123)¹⁸ and only ca $0.04 \times (1/4)$ for optimally doped Bi-2212¹⁷. Since $F \sim I_M$ enters Eq. 2 in the product $g^2 F$, however, we continue to use Eq. 35 for simplicity keeping in mind that the actual value of the coupling constant required is an order of magnitude higher than the one of Table 1.

Let us make here a short comment on a recent discussion regarding the small experimental values of I_M . Kee,

Kivelson, and Aeppli⁵¹ claimed that they are too small for the mode to play any significant role. Abanov *et al.*⁵² in their response to the criticism argued that even though I_M is small, the mode can lead to large selfenergy effects because it is rather narrow in \mathbf{q} space. There is another argument justifying the “mode models”. As mentioned above $F \sim I_M$ appears in Eq. 2 only in the product $g^2 F$. The susceptibility χ_{RM} normalized to 1/4, as in our calculations, together with $g = 0.35$ eV, will be shown to lead to results that are to some extent in agreement with experimental data. The same results could also be obtained using “the true χ_{RM} ”, i.e., χ_{RM} normalized to the experimental value of 0.002 (0.009), with $g \approx 4$ eV ($g \approx 2$ eV). The important point is that the latter values of g are not unrealistic given Eq. 1 and the high values of U expected to be relevant for the HTCS. It is thus well possible that, inspite of the small values of I_M , the selfenergy effects due to the mode are large. The fact, however, that its spectral weight is small as compared to that of the SF continuum implies that only some low energy features can be attributed to the mode. The intermediate energy-scale spectra must be determined rather by the continuum.

D. Computational details

The results presented in this work have been obtained using two different codes. In the first one, the finite linewidth of the resonance is taken into account, the second one is adapted to the case of the sharp resonance. The calculations proceed essentially in three steps.

(i) In the first step, the self-energies and spectral functions of selected \mathbf{k} -points are computed by using Eqs. 16 and 15. First we concentrate on the frequency integration of Eq. 16. Within the sharp resonance approach, it is trivial due to the δ function in Eq. 34. The structures of the resulting function, however, are sharp and the sampling of the subsequent BZ integration must be very dense. Within the broad resonance calculation, the integral of Eq. 16 is divided into two parts: the part containing the Bose factors in the numerators of Eq. 17 and the one containing the remaining terms. The latter part can be expressed analytically but the former one has to be calculated numerically. For this purpose, we have used the grid containing 500 ω -points ranging from $\omega = 0$ to $\omega = 10k_B T/\hbar$. Due to the separable form of χ_{RM} , the same frequency integrals occur for any $\mathbf{k} \in 1.$ BZ. This has allowed us to compute their values once and for all

at the beginning.

Next, we focus on the BZ integration. The dispersion relation is nontrivial and the structure in the susceptibility relatively sharp. In addition, a discussion of the singularities requires the spectral functions to be continued very close to the real axis: a typical value of δ in Eq. 15 is only 0.05 meV. For all these reasons a very fine grid (typically 300×300 for the broad resonance and 1000×1000 for the sharp one) is needed for the BZ integration. Without further simplifications the calculations of the infrared conductivity would be fairly time consuming: they would require elaborate integrations for all \mathbf{k} -points of the corresponding grid. This problem can be partially overcome by using an approximation described below. The BZ integral of Eq. 16 can be schematically written as

$$\int_{2D BZ} d\mathbf{q} \zeta(\mathbf{q}) D(\mathbf{k} + \mathbf{q}, iE_n), \quad (36)$$

where ζ is the \mathbf{q} dependent part of B and D is a function of $\mathbf{k} + \mathbf{q} = \mathbf{k}'$ and iE_n . Using the \mathbf{k} -space periodicity of both ζ and D we obtain

$$\int_{2D BZ} = \int_{2D BZ} d\mathbf{k}' \zeta(\mathbf{k}' - \mathbf{k}) D(\mathbf{k}', iE_n). \quad (37)$$

The idea underlying our approximation is that ζ is a smooth function as compared to D . This allows us to use the approximation

$$\int_{2D BZ} \approx \sum_{ij} \zeta(\mathbf{k}_{ij} - \mathbf{k}) D_{ij}(iE_n), \quad (38)$$

where $i = 1, 2, \dots N_1$, $j = 1, 2, \dots N_1$, N_1 specifies the number of \mathbf{k} -points in the auxiliary grid (typically $N_1 = 30$), $\mathbf{k}_{ij} = (k_{xi}, k_{yi})$, $k_{xi} = (2i-1)\pi/(aN_1)$, $k_{yi} = (2j-1)\pi/(aN_1)$, and

$$D_{ij}(iE_n) = \int_{2(i-1)\pi/(aN_1)}^{2i\pi/(aN_1)} \int_{2(j-1)\pi/(aN_1)}^{2j\pi/(aN_1)} d\mathbf{k} D(\mathbf{k}, iE_n). \quad (39)$$

The quantities $D_{ij}(iE_n)$ have been computed once and for all at the beginning, using grids of typically 10×10 (30×30) \mathbf{k} -points for the broad (sharp) resonance.

(ii) In the second step, the contributions of selected \mathbf{k} -points to the real part of the (isotropic) in-plane infrared conductivity are calculated. We define the contribution of a \mathbf{k} -point as (cf. Eq. 31)

$$\Delta\sigma_1(\mathbf{k}, \omega) = \frac{e^2}{2\omega} \frac{N_p}{da^2} [v_x^2(\mathbf{k}) + v_y^2(\mathbf{k})] \int \frac{dE}{2\pi} \text{Tr} [A(\mathbf{k}, E) A(\mathbf{k}, E + \hbar\omega)] \times [n_F(E) - n_F(E + \hbar\omega)]. \quad (40)$$

The computation of the convolution of the spectral func-

tions in Eq. 40 is again very demanding because the sharp

quasiparticle peaks must be handled correctly. Typically a grid of at least 5000 energy-points for a spectrum ranging up to 300 meV is required. In the calculations of Subsecs. IV E and IV F, where the sharp spectral structures are not at the centre of interest, the spectral functions have been continued only to a distance of typically 1 meV from the real axis and energy grids of typically 6000 points for spectra ranging up to 3 eV have been used.

(iii) The calculation of $\sigma_1(\omega)$ is completed by the BZ integration of $\Delta\sigma_1$:

$$\sigma_1(\omega) = 4a^2 \int_{2D \text{ IBZ}} d\mathbf{k} \Delta\sigma_1(\mathbf{k}, \omega), \quad (41)$$

where IBZ stands for the irreducible part of the BZ. The integration is relatively simple because the functions $\Delta\sigma_1$ are already fairly smooth. The grid of 200×200 \mathbf{k} -points in the full BZ, i.e., ca 5000 \mathbf{k} -points in its irreducible part, proved to be sufficient.

If not specified in the text, the computations are performed for $T = 20$ K.

IV. RESULTS AND DISCUSSION

The infrared spectra will be analyzed in terms of the quasiparticle spectral functions. For this reason, we first present and discuss, as a necessary prerequisite, our calculated spectral functions of some representative \mathbf{k} -points (Subsec. IV A) and their contributions to the real part of the conductivity (Subsec. IV B). The main new results of the paper will then be presented in Subsects. IV C-IV F.

A. Quasiparticle spectral functions

Figure 2 shows the spectral functions (more precisely, the first diagonal elements of the matrix (15), i.e., the “true” spectral functions) of three points located at the Fermi surface (the points CS, B, and HS) and of the X-point. The spectra exhibit quasiparticle peak(s) (one for the CS and two for the other points, where the magnitude of the superconducting gap is finite), that would appear already for the (noninteracting) BCS ground-state, and incoherent broad satellites at higher energies, that are due to the interaction. The structures are more pronounced in the spectra for $\Gamma = 0$. The latter are thus more suitable for a discussion of the singularities.

The energies of the quasiparticle peaks labelled Q and Q' (see Fig. 2) are -8 meV (CS, the nonzero value is due to a slight renormalization of the Fermi surface caused by the interaction), ± 22 meV (B), ± 35 meV (HS), and ± 37 meV (X). The magnitude of the values for the HS is larger than Δ_0 which reflects an enhancement of superconductivity due to the coupling to the mode.

Next we discuss the incoherent parts of the spectral functions. For all of the \mathbf{k} -points, three onset features can be resolved at negative energies, denoted by R, S, and T

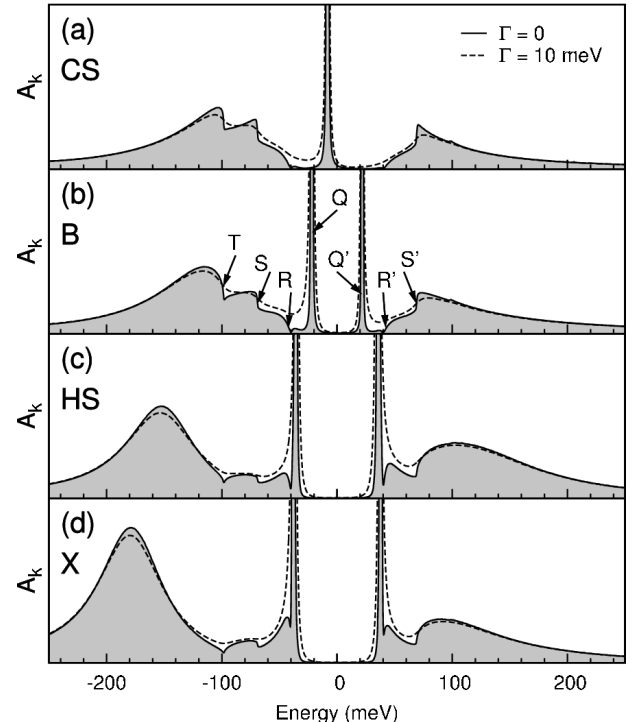


FIG. 2: Spectral functions of the \mathbf{k} -points defined in Fig. 1. The notation of spectral structures is introduced in panel (b).

(see Fig. 2), and two at positive energies (R', S'). Interestingly, their positions are the same for all the \mathbf{k} -points: the feature $R(R')$ is located at $-(+)\hbar\omega_0$ [∓ 40 meV], $S(S')$ at $-(+)\hbar\omega_0 + \Delta_A \approx -(+)\hbar\omega_0 + \Delta_0$ [$\approx \mp 70$ meV] and T at $-|\hbar\omega_0 + E_X|$, where $E_X = \sqrt{\epsilon_X^2 + \Delta_X^2} \approx -100$ meV. The physical meaning of the structures S, S', and T has been discussed in detail by Eschrig and Norman²⁰; their analysis also yields the formulas for the energies of the features. The structures R and R', which are well resolved only for $\Gamma = 0$, correspond to final states involving a nodal quasiparticle and the magnetic excitation. The energy of the broad maximum at negative energies, below the feature T, is \mathbf{k} -dependent. Its values are -100 meV (CS), -115 meV (B), -150 meV (HS), and -180 meV (X). The decrease of the energy when going from the CS to the X-point is accompanied by a systematic increase of the spectral weight.

In order to illustrate the role of the input parameters, we compare in Fig. 3 the results presented above with those obtained using the parametrizations of the dispersion relation and of the magnetic susceptibility and the values of Δ_0 (35 meV), $g = 0.65$, and T (40 K) of Ref. 20. Note first that the reference spectra are in good agreement with those of Ref. 20. Note further, that for small absolute values of energy, the two sets of spectra are very similar. On the other hand, the positions and shapes of the lowest incoherent peak are fairly different. This is due to the fact that the value of the effective coupling constant used by Eschrig and Norman is considerably smaller than ours⁵³. The difference in the energy of

the onset of the latter peak (ca -100 meV in this work, ca -90 meV in Ref. 20) is related to the difference in the location of the X-point with respect to the Fermi surface (see Fig. 1).

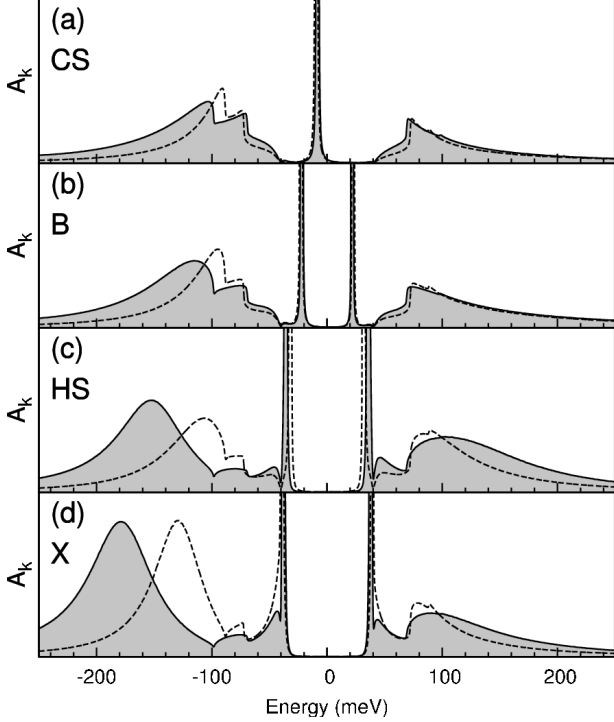


FIG. 3: Spectral functions from Fig. 2 (solid lines) compared with those obtained using the values of the input parameters of Ref. 20 (dashed lines).

B. Contributions of the selected \mathbf{k} -points to $\sigma_1(\omega)$

The contributions of the \mathbf{k} -points labelled as CS, B, and HS to $\sigma_1(\omega)$ are shown in Fig. 4. The contribution of the X-point is identically zero because $\nu(X) = 0$. In the following, the structures of the functions will be discussed in terms of those of the corresponding spectral functions. Such a discussion is straightforward only for the normal state, where the expression on the r. h. s. of Eq. 31 reduces to a convolution of the (true) spectral functions. For the superconducting state, the off-diagonal components of the spectral-function matrix (15) play a crucial role. For example, the transitions $Q \rightarrow Q'$ do not contribute because of a precise cancellation of the term on the r. h. s. of Eq. 31 containing the diagonal components and that containing the off-diagonal components. Other transitions between occupied and unoccupied states, however, do show up in the conductivity spectra, only their spectral weights are influenced by the presence of the off-diagonal components.

Three singularities (discontinuities of the first derivative), can be observed in the spectra. In Fig. 4 they

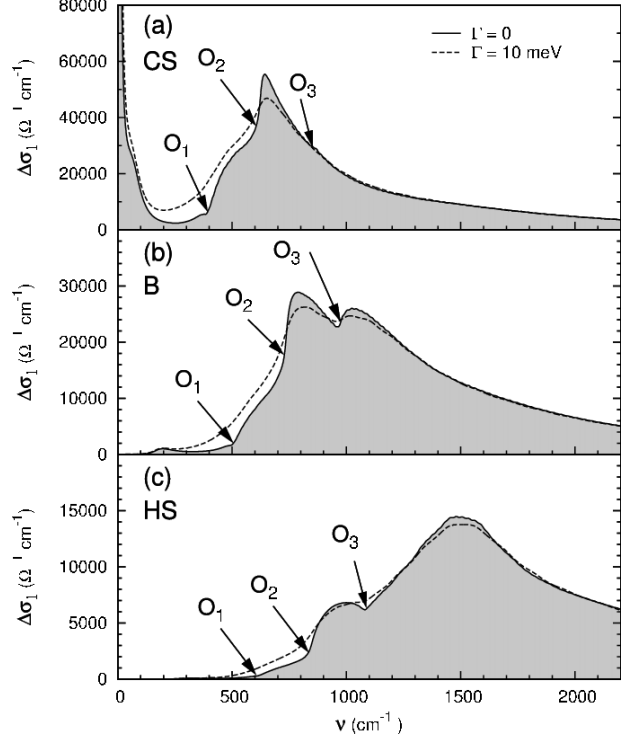


FIG. 4: Contributions of the selected \mathbf{k} -points to the real part of the optical conductivity. The onset features are marked by the arrows.

are marked by the arrows. The onset feature O_1 corresponds to the transitions $Q \rightarrow R'$ and $R \rightarrow Q'$ (for the CS, $Q \equiv Q'$). It appears at the energy of $\bar{E}_k + \hbar\omega_0$, where \bar{E}_k is the energy of the quasiparticle peak. The values of the corresponding wavenumbers are 380 cm^{-1} , 500 cm^{-1} , and 600 cm^{-1} for the points CS, B, and HS, respectively. The second onset feature O_2 is related to the transitions $Q \rightarrow S'$ and $S \rightarrow Q'$. It is shifted with respect to O_1 approximately by Δ_0 , the values of the corresponding wavenumbers are 620 cm^{-1} , 740 cm^{-1} , and 840 cm^{-1} , respectively. The third discontinuity of the first derivative labelled O_3 can be traced back to the transition $T \rightarrow Q'$. It is shifted with respect to O_1 by E_X , the values of the corresponding wavenumbers are 850 cm^{-1} , 970 cm^{-1} , and 1070 cm^{-1} , respectively. Small structures at very low energies in parts (b) and (c) of Fig. 4 are artefacts due to an incomplete continuation to the real axis. The contribution of the cold spot requires a more careful discussion. Besides the features O_1 , O_2 , and O_3 , it contains a Drude-like component at very low energies. Its presence is related to the fact that at this point the superconducting gap vanishes. Some structures around 60 cm^{-1} and 320 cm^{-1} are due to transitions between the maximum of the quasiparticle peak Q located at -8 meV and its tail ranging to $E = 0$, and between the tail and the structures R, R' , respectively. The spectral weight associated with the transition $T \rightarrow Q'$ is small because only the tail of the quasiparticle peak participates. It can be

seen in Fig. 4 that the spectra for finite Γ are similar to those of $\Gamma = 0$, the onset features, however, are by far less pronounced.

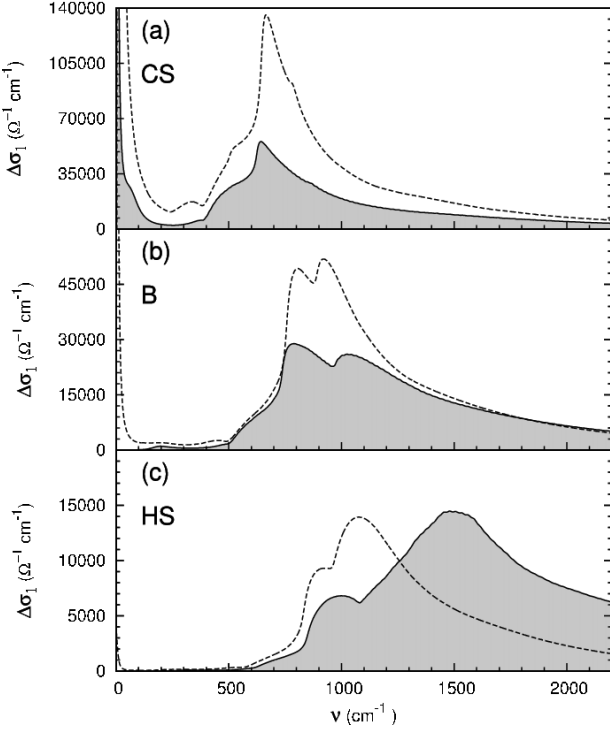


FIG. 5: Contributions of the selected \mathbf{k} -points to the real part of the optical conductivity from Fig. 4 (solid lines) compared with those obtained using the values of the input parameters of Ref. 20 (dashed lines).

For reference, we compare in Fig. 5 the results presented above with those obtained using the values of the input parameters of Ref. 20 (the values of a , d and δ have not been changed). It can be seen that the frequencies of the singularities are fairly close to each other, except for O_3 . The discrepancy can be traced back to the difference in the location of the Fermi surface. The differences in the absolute values reflect those of the dispersion relation and of the coupling constant.

The contribution of the hot spot shown in the bottom panels of Figs. 4 and 5 can be compared with $\sigma_1(\omega)$ resulting from the model of ACS, shown in Fig. 2 of Ref. 33. The latter exhibits a sharp onset feature at $2\Delta_0 + \hbar\omega_0$, a maximum around $5\Delta_0$, and a gradual decrease at higher frequencies. Our spectra display all these features. The onset is labelled as O_2 . The maximum is located at about 1500 cm^{-1} for our values of the input parameters and at ca 1100 cm^{-1} for those of Ref. 20, its frequency strongly depends on the value of g . The main differences are: (a) In the spectra of Ref. 33, $\sigma_1 = 0$ for frequencies below the onset. In our spectra, $\Delta\sigma_1$ acquires nonzero values already above the first onset frequency of $\sim \Delta_0 + \hbar\omega_0$. The discrepancy is due to the fact that ACS neglected excitations involving nodal quasiparticles. (b) In our spectra, the onset O_2 is followed by another one at ca

$\Delta_0 + E_X + \hbar\omega_0$ (O_3). Its absence in the spectra of Ref. 33 is due to the fact that details of the dispersion relation have been neglected.

In summary, the contribution of a \mathbf{k} -point to $\sigma_1(\omega)$ exhibits three onset features, whose energies are $\bar{E}_\mathbf{k} + \hbar\omega_0$, ca $\bar{E}_\mathbf{k} + \Delta_0 + \hbar\omega_0$, and $\bar{E}_\mathbf{k} + \hbar\omega_0 + E_X$.

C. Real part of the optical conductivity and the origin of the onset feature around ω_0

So far we have discussed singularities that appear in the contributions to $\sigma_1(\omega)$ of the individual \mathbf{k} -points. It is important to find out how do these singularities manifest themselves in the spectra of the total conductivity. Here we shall show that the feature O_1 of Fig. 4 gives rise to a clear onset of σ_1 starting around ω_0 . The singularities labelled as O_2 and O_3 cannot be clearly resolved in the spectra themselves, the former one, however, can be uncovered by means of numerical differentiation. This will be shown in the next subsection.

Figure 6 shows the spectra of $\sigma_1(\omega)$ (upper panel) and the contributions of the three regions of the irreducible BZ defined in Fig. 7 (bottom panel). The imaginary part

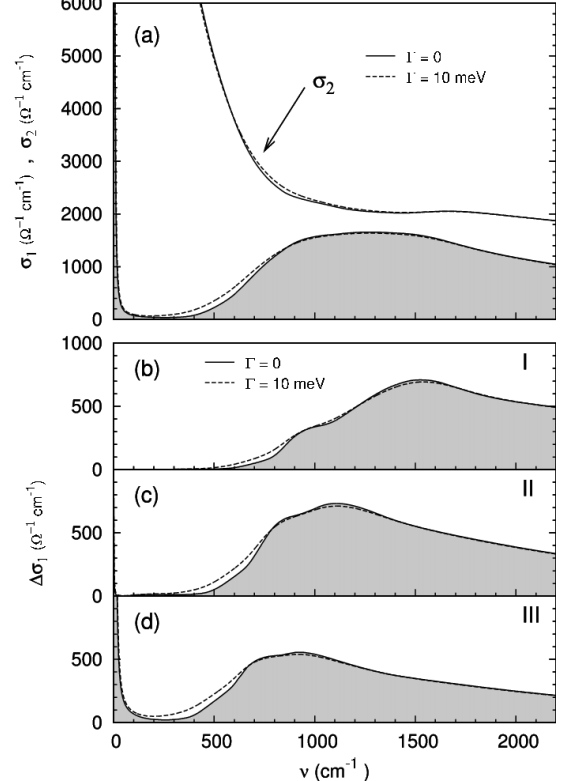


FIG. 6: Real and imaginary parts of the optical conductivity (upper panel) and the contributions to $\sigma_1(\omega)$ of the three regions of the irreducible BZ defined in Fig. 7 (bottom panel).

$\sigma_2(\omega)$ has been obtained by using Eq. 26. The values of ω_{pl} and $\omega_{\text{pl,sc}}$ obtained by using Eq. 27 and Eq. 28 are 17800 cm^{-1} and 12100 cm^{-1} , respectively. Interestingly,

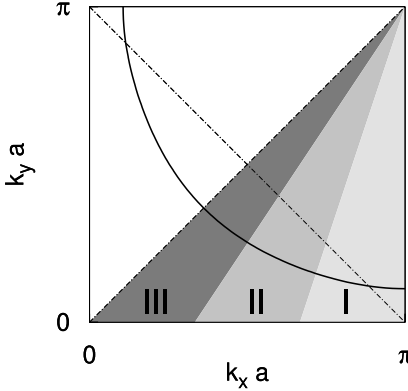


FIG. 7: Three regions of the irreducible BZ used in the discussion of the total conductivity.

the magnitudes of the three contributions to $\sigma_1(\omega)$ in the infrared are comparable. This is a result of a competition between the velocity factor in Eqs. 31, 40, which is higher for the quasiparticles around the BZ diagonal (region III), and the density of states at the Fermi surface, which is higher in region I. It appears that the characteristic singularities discussed in the previous subsection can still be resolved in the spectra of the bottom panel. For example, the contribution of region I still contains the onset features O_1 , O_2 , and O_3 characteristic of the hot spot. In the spectra of the total conductivity, however, they are approximately averaged out and cannot be clearly resolved, except for the first onset feature: σ_1 is rather small above the narrow Drude peak and below ω_0 and it starts to increase at ω_0 (or, for finite Γ , around ω_0). The bottom panel of Fig. 6 shows that the onset originates in region III. It can be attributed to the lowest allowed transitions ($Q \rightarrow R'$ and $R \rightarrow Q'$) of the region around the nodes. The shape of the onset can thus be expected to depend on the behavior of $\Delta_{\mathbf{k}}$ in the proximity of the nodes. In order to explore this dependence, we have performed the computations for the following three forms of the superconducting gap:

$$\Delta_{\mathbf{k}} = \frac{\Delta_0}{2} [\cos(k_x a) - \cos(k_y a)]^{\gamma} \quad (42)$$

with $\gamma = 0.5, 1, 3$ (for $\gamma = 0.5$ the signs have to be properly adjusted). The results are shown in Fig. 8. They can be interpreted as follows: the larger (smaller) the value of the exponent γ , the wider (narrower) the region around the BZ diagonal, where the magnitude of the superconducting gap is small, and the larger (smaller) the spectral weight right above ω_0 originating in this region. The increase (decrease) of γ thus effectively results in a red (blue) shift of the onset.

For reference, we again compare in Fig. 9 the results presented above with those obtained using the values of the input parameters of Ref. 20; the corresponding values of ω_{pl} and $\omega_{\text{pl,sc}}$ are 17900 cm^{-1} and 12700 cm^{-1} , respectively.

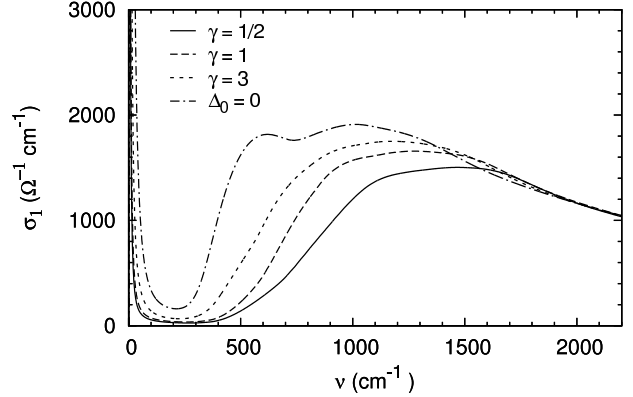


FIG. 8: Real part of the optical conductivity for the three forms of the superconducting gap of Eq. 42. Also shown is the result for $\Delta_k = 0$.

D. Parameters of the extended Drude model, effective spectral function $W(\omega)$ and the origin of its main maximum

A common way to discuss the in-plane infrared spectra is in terms of the scattering rate $[1/\tau](\omega)$ and the mass enhancement factor $[m^*/m](\omega)$. These quantities are defined by the so called extended Drude model^{24,32}:

$$\sigma(\omega) = \varepsilon_0 \frac{\omega_{\text{pl}}^2}{[1/\tau](\omega) - i\omega[m^*/m](\omega)}. \quad (43)$$

Their physical significance relies on a close relation between the optical selfenergy,

$$S^{opt}(\omega) = \frac{1}{2} \left(\omega \left[1 - \frac{m^*}{m}(\omega) \right] - \frac{i}{\tau}(\omega) \right), \quad (44)$$

and the (true) quasiparticle selfenergy (for a recent discussion see Ref. 54). The calculated spectra of $1/\tau$ and m^*/m are shown in Fig. 10. They have been extracted from those of σ_1 and σ_2 using the following formulas resulting from Eq. 43:

$$\frac{1}{\tau}(\omega) = \omega_{\text{pl}}^2 \varepsilon_0 \frac{\sigma_1(\omega)}{\sigma_1^2(\omega) + \sigma_2^2(\omega)}, \quad (45)$$

$$\frac{m^*}{m}(\omega) = \frac{\omega_{\text{pl}}^2 \varepsilon_0}{\omega} \frac{\sigma_2(\omega)}{\sigma_1^2(\omega) + \sigma_2^2(\omega)}. \quad (46)$$

The trends in the spectra of $1/\tau$ and m^*/m can be easily related to those of σ_1 and σ_2 . The obvious similarity between the spectra of $1/\tau$ and those of $\sigma_1(\omega)$, for example, can be interpreted as follows. At low frequencies (a) $\sigma_2 \gg \sigma_1$ and (b) σ_2 is dominated by the singular term, $\varepsilon_0 \omega_{\text{pl,sc}}^2 / \omega$ (see Fig. 6). As a consequence, $[1/\tau](\omega)$ is approximately proportional to $\omega^2 \sigma_1(\omega)$ (see Eq. 45). This explains the similarity. The latter allows us to consider derivatives of $[1/\tau](\omega)$ instead of those of $\sigma_1(\omega)$ when searching for the singularities.

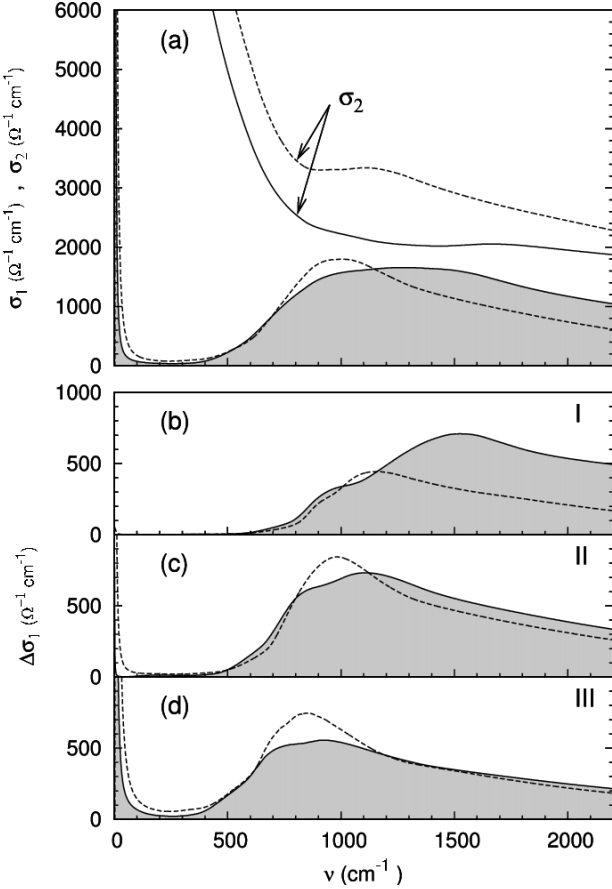


FIG. 9: Real and imaginary parts of the optical conductivity (upper panel) and the three components of $\sigma_1(\omega)$ (bottom panel) from Fig. 6 (solid lines) compared with those obtained using the values of the input parameters from Ref. 20 (dashed lines).

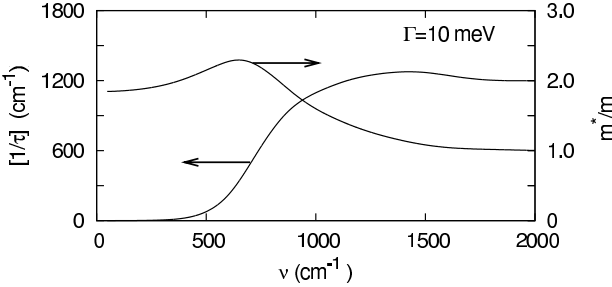


FIG. 10: Spectra of the scattering rate and the mass enhancement factor extracted from those of σ_1 and σ_2 shown in Fig. 6.

Recently, it has become popular^{26,31,55,56,57,58} to use the function $W(\omega)$ of Eq. 6 which is related to $[1/\tau]$ as

$$W(\omega) = \frac{1}{2\pi} \frac{d^2}{d\omega^2} \left[\omega \frac{1}{\tau}(\omega) \right]. \quad (47)$$

This has been motivated by the theoretical works of CSB³¹ and ACS³³ discussed in the introduction. We recall that according to CSB the most pronounced maxi-

mum of $W(\omega)$ reveals the spectral function of the bosons, that are coupled to the charged quasiparticles (shifted by Δ_0 , see Eq. 6). Within the resonant mode scenario, the maximum should thus be located at $\Omega_{\text{CSB}} = \Delta_0 + \hbar\omega_0$. According to the strong-coupling SF-based theory of ACS $W(\omega)$ should exhibit three singularities at $2\Delta_0 + \hbar\omega_0$, $4\Delta_0$, and $2\Delta_0 + 2\hbar\omega_0$ (see Fig. 3 of Ref. 33). The first singularity, which is the most pronounced one, is due to the first onset of $\sigma_1(\omega)$ (see Fig. 2 of Ref. 33 and the discussion in Subsect. IV B). It consists of a sharp maximum followed by a minimum.

Here we shall follow the strategy of the preceding subsections and attempt to interpret the structures of $W(\omega)$ in terms of the quasiparticle spectral functions and the corresponding contributions to $\sigma_1(\omega)$. Our most important finding is that the main maximum of $W(\omega)$ can be associated with the onset feature O_2 of parts (a) and (b) of Fig. 4, i.e., with the appearance (above the characteristic frequency of the maximum) of final states consisting of a quasiparticle from the nodal region, a quasiparticle from the antinodal region, and the resonance mode.

Figure 11 shows our calculated spectra of $W(\omega)$ (upper panel) and contributions to W of the three regions defined in Fig. 7 (bottom panel). The contribution of a region is defined by

$$\Delta W(\omega) = \frac{\varepsilon_0 \omega_{pl}^2}{2\pi} \frac{d^2}{d\omega^2} \left[\omega \frac{\Delta\sigma_1(\omega)}{\sigma_1^2(\omega) + \sigma_2^2(\omega)} \right]. \quad (48)$$

The spectra of the quantities in the square brackets of Eqs. 47 and 48 have been smoothed before taking the second derivatives, a typical scale of the smoothing being 3 meV. First we discuss the spectra of the bottom panel. Each contribution exhibits three maxima (M_1 , M_2 , M_3) separated by two minima (M'_1 , M'_2). The corresponding frequencies are 800 cm^{-1} , 1090 cm^{-1} , 1800 cm^{-1} , 910 cm^{-1} , 1500 cm^{-1} (I), 680 cm^{-1} , 950 cm^{-1} , 1620 cm^{-1} , 830 cm^{-1} , 1130 cm^{-1} (II), 600 cm^{-1} , 880 cm^{-1} , 1030 cm^{-1} , 770 cm^{-1} , 940 cm^{-1} (III). Spectral features above the frequency of the third maximum are weak. It can be relatively easily seen that the maxima M_1 and M_2 correspond to the onset features O_2 and O_3 , respectively (see Figs. 4 and 6) and that the minimum M'_2 is related to the maximum of $\Delta\sigma_1(\omega)$ in mid-infrared (see Fig. 6). The structures M'_1 and M_3 can be interpreted analogously. Next we concentrate on the upper panel. The spectra of $W(\omega)$ exhibit a pronounced maximum at $\sim 620 \text{ cm}^{-1}$, a minimum at $\sim 870 \text{ cm}^{-1}$, weak structures in the range from 1000 cm^{-1} to 1400 cm^{-1} , and a minimum around 1500 cm^{-1} . All these features can be interpreted in terms of constructive or destructive interference of the three contributions. In particular, the main maximum originates from the structures M_1 (III) and M_1 (II), the latter being partially compensated by M'_1 (III). Note the important role played by the negative contribution of the zone III. The frequency of the maximum Ω_M (here 620 cm^{-1}) appears to be slightly higher than $\omega(M_1, III) \approx \omega(O_2, III)$ (here

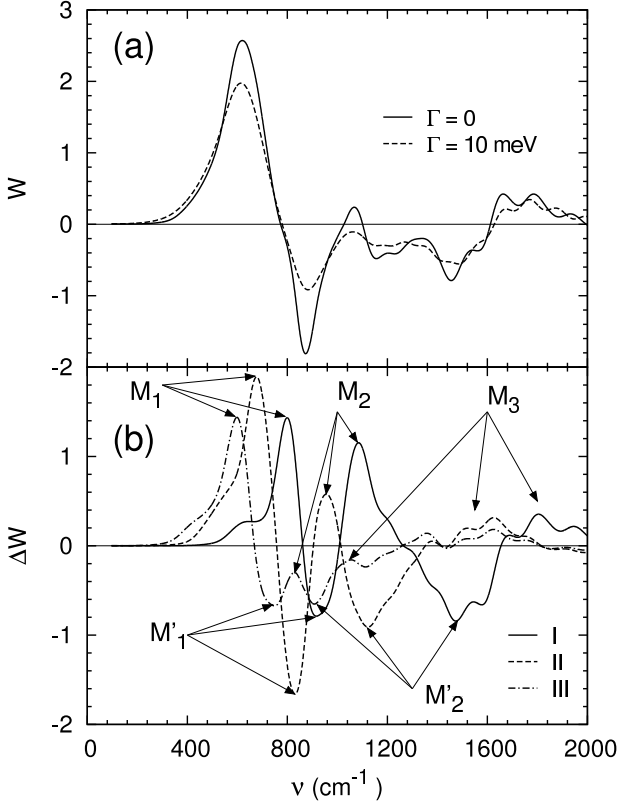


FIG. 11: Spectra of the function $W(\omega)$ defined by Eq. 6 obtained from the conductivities of Fig. 6 (upper panel). Bottom panel: the contributions of the three regions defined in Fig. 7.

600 cm⁻¹). The latter frequency is further slightly higher than $\omega(O_2, CS) \approx (\Delta_0/\hbar) + \omega_0$ (565 cm⁻¹). Our general conclusion is that Ω_M is somewhat larger than $\Omega_{CSB} = (\Delta_0/\hbar) + \omega_0$ but much smaller than $2(\Delta_0/\hbar) + \omega_0$. The magnitude of the difference, $\Omega_M - (\Delta_0/\hbar) - \omega_0$, depends on details, e.g., on the shape of the superconducting gap. In our case we have $\Omega_M - (\Delta_0/\hbar) - \omega_0 = 55$ cm⁻¹. The conclusion should be valid for any sharp bosonic mode which couples the nodal regions to the antinodal ones. It can be easily seen that the shape of the maximum does not correspond to the neutron peak. The FWHM is about 170 cm⁻¹ and about 210 cm⁻¹ for $\Gamma = 0$ and $\Gamma = 10$ meV (ca 80 cm⁻¹), respectively.

Figure 12 shows the results obtained using the values of the input parameters of Ref. 20. The main differences between the spectra of the bottom panels of Fig. 11 and Fig. 12 are: (a) The maxima M_1 and M_2 are closer to each other in Fig. 12 than in Fig. 11. (b) The maximum M_3 is located at lower energies in Fig. 12 than in Fig. 11. These differences can be traced back to those in the position of the Fermi level and in the value of the coupling constant. The frequency of the main maximum in the upper panel of Fig. 12 is approximately the same as that of Fig. 11, in agreement with our general conclu-

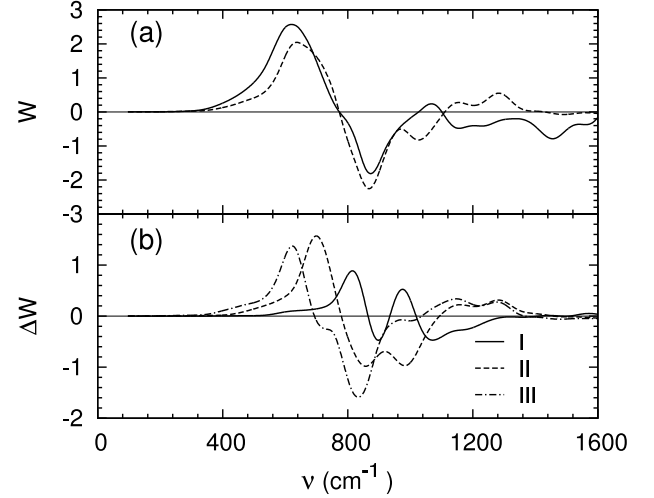


FIG. 12: (a) The $\Gamma = 0$ meV spectrum of $W(\omega)$ from Fig. 11 (solid line) together with the one corresponding to the values of the input parameters from Ref. 20 (dashed line). (b) The same as in Fig. 11 (b) but for the values of the input parameters from Ref. 20.

sion presented above. The shape of the maximum and the spectral structures at higher energies, however, differ considerably.

E. Role of the spin-fluctuation continuum

So far we have considered the spin susceptibility in the resonant-mode form of Eq. 4. Such an approach may suffice to provide an understanding of the spectral features discussed in the preceding subsections: the onset of $\sigma_1(\omega)$ around ω_0 and the main maximum of $W(\omega)$. It is well known, however, that the spectral weight of the resonant mode is much smaller than that of the spin-fluctuation continuum. The overall shape of the optical response, in particular in the mid-infrared region, can thus be expected to be determined by the continuum rather than by the mode. The inadequacy of the resonant-mode approach to reproduce the mid-infrared data can indeed be seen by comparing the computed scattering rate spectra with those deduced from experimental data^{27,29} and called “experimental (scattering rate) spectra” in the following⁵⁹. In the spectra of Fig. 10, $1/\tau$ saturates above 1200 cm⁻¹ at a value of about 1200 cm⁻¹ and it decreases at higher frequencies (to be shown below). In the experimental spectra, on the other hand, $1/\tau$ saturates only above ~ 5000 cm⁻¹, at a value of several thousands cm⁻¹.

Here we report on our attempts to understand the experimental data in terms of a model where the spin susceptibility contains, in addition to the resonant mode, a very broad continuum term:

$$\chi(\mathbf{q}, \omega) = b_M \chi_{RM}(\mathbf{q}, \omega) + b_C \chi_C(\mathbf{q}, \omega), \quad (49)$$

where χ_{RM} is given by Eq. 4 with $\Gamma = 10\text{meV}$ in conjunction with Eq. 35 and

$$\chi_C(\mathbf{q}, \omega) = \frac{1}{1 + (\mathbf{q} - \mathbf{Q})^2 \xi_C^2} \frac{F_C}{\omega_C^2 - \omega^2 - i\Gamma_C \omega} \quad (50)$$

is the continuum component with the same structure as χ_{RM} . The values of the parameters of χ_C used in our calculations are: $\xi_C = 2\text{\AA}$ (i.e., about one half of the value of the lattice parameter), $\omega_C = 400\text{meV}$ (this choice will be motivated below), $\Gamma_C = 1000\text{meV}$, and the value of F_C is determined by Eq. 35. The spectra of both components are shown in Fig. 13 (a). A similar continuum component has been considered by Schachinger, Tu, and Carbotte³⁷ in their discussion of the scattering rate in Bi-2212. The parameters b_M and b_C in Eq. 49 express the spectral weights of the two components. Figure 14

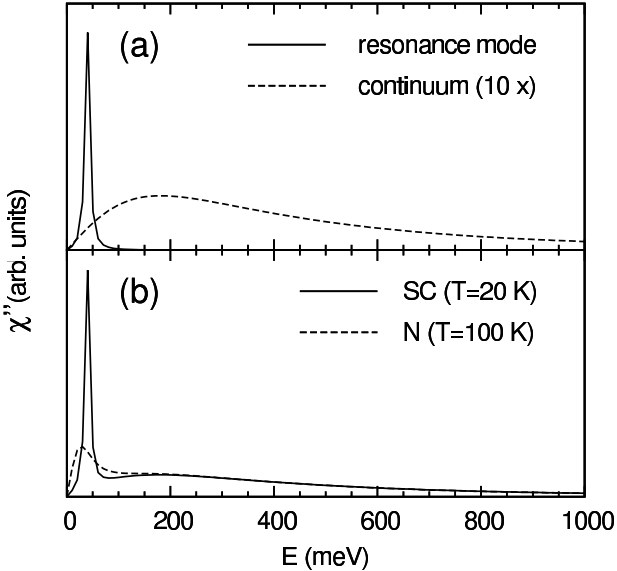


FIG. 13: (a) The (q-integrated) spectra of the imaginary part χ'' of the spin susceptibility corresponding to the resonance mode (solid line) and to the continuum term introduced in Eq. 50 (dashed line), respectively. (b) Those used as a starting point in the computations of Subsec. IV F. The solid and the dashed line correspond to the superconducting state ($T = 20\text{ K}$) and to the normal state ($T = 100\text{ K}$), respectively.

shows the b_M - and b_C -dependence of $\sigma_1(\omega)$ and $[1/\tau](\omega)$. The low frequency parts of the spectra shown as the solid lines in panels (a₁) and (a₂), have already been presented above in Figs. 6 and 10. Note that in the mid-infrared region (a) σ_1 decreases with increasing frequency much faster than in the experimental spectra and (b) $1/\tau$ also decreases, in contrast to the experimental spectra. The right panel of Fig. 14 clearly demonstrates the distinct roles of the two components: (i) The mode yields a relatively sharp onset of $1/\tau$ centered at about Ω_M , followed by a gradual decrease. (ii) The continuum leads to an approximately linear increase followed by a plateau above $\sim 4000\text{cm}^{-1}$. As shown in Fig. 15, the onset frequency

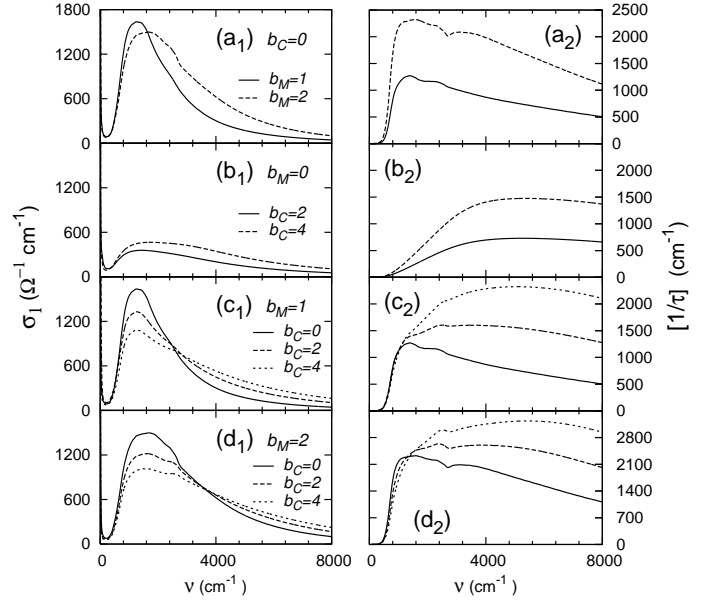


FIG. 14: The conductivity and the scattering rate as functions of the parameters b_M and b_C expressing the spectral weights of the mode and the continuum, respectively.

of the plateau reflects the width of χ_C , which is here determined by ω_C of Eq. 50. Our choice of the value of

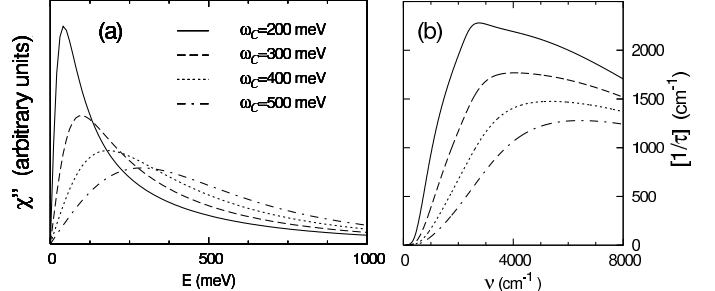


FIG. 15: The (q-integrated) imaginary part χ'' of the spin susceptibility (a) and the scattering rate (b) as functions of the parameter ω_C introduced in the text.

ω_C has been motivated by the experimental spectra of Refs. 27 and 29. (iii) It can be seen that $1/\tau$ is approximately a linear function of b_M and b_C . For example, $[1/\tau](b_M = 1, b_C = 4)$ [dotted line in part (c₂)] is approximately equal to $[1/\tau](b_M = 1, b_C = 0)$ [solid line in part (a₂)] + $[1/\tau](b_M = 0, b_C = 4)$ [dashed line in part (b₂)]. The value of b_M (b_C) determines the value of $1/\tau$ above the sharp onset or, in other words, the height of the step in $1/\tau$ (the difference between the value of $1/\tau$ of the plateau and the height of the step). (iv) The spectra for $b_M \neq 0$ exhibit an additional structure around 2500cm^{-1} . It can be shown, along the lines of Subsect. IV B, to be connected to a singularity in the density of the relevant final states located approximately at

$$\hbar\omega_S = \mu - \epsilon_\Gamma + \Delta_0 + \hbar\omega_0. \quad (51)$$

The latter is related to the van Hove singularity associated with the bottom of the band at the Γ -point. The frequency ω_S can thus be used to estimate $\mu - \epsilon_\Gamma$, i.e., the width of the occupied part of the band. It is very interesting that the experimental scattering rate spectra, both for Y-123 and for Bi-2212, display a fine structure around 3000 cm^{-1} , which is similar to that appearing in the computed spectra. The similarity leads us to speculate that it has the same origin, i.e., that it is due to the singularity of the density of states discussed above. The value of $\mu - \epsilon_\Gamma$ of $\sim 0.3\text{ eV}$ resulting from Eq. 51 is in rough agreement with the photoemission values of 0.25 eV (Y-123, Ref. 60) and 0.40 eV (Bi-2212, Ref. 21). According to the proposed interpretation, the structure should become less pronounced above T_c because of the disappearance of the sharp mode. In the experimental spectra, however, it seems to be only weakly temperature dependent. At present we are not aware of any explanation of this discrepancy.

It can be seen that the experimental spectra can be approximately reproduced only by taking a value of b_M of around 1.0 and a considerably higher value of b_C . For $b_M = 1.0$ and $b_C = 4.0$, e.g., the calculated spectra are in reasonable agreement with those of optimally doped Y-123 from Ref. 29. In order to reproduce the spectra of optimally doped Bi-2212 from Ref. 27 a higher value of b_C (ca 10) has to be taken. Let us note that the values of the ratio b_C/b_M under consideration are still smaller than those suggested by the neutron scattering experiments^{17,18}.

F. Some aspects of the temperature dependence of the spectra

In Subsubsect. IV F 1 we present and discuss a computed temperature dependence of the spectra characteristic of the spin-fluctuation scenario, which may be helpful for understanding the experimental data. In Subsubsect. IV F 2 we then focus on the temperature dependence of the intraband spectral weight.

1. Temperature dependence of the infrared spectra characteristic of the spin-fluctuation scenario

Figure 16 shows the spectra of σ_1 , $1/\tau$ and m^*/m computed for three temperatures: $T = 20\text{ K}$ (superconducting state), $T = 100\text{ K}$, and $T = 200\text{ K}$ (normal state). For each temperature, the value of the chemical potential was adjusted to yield the total number of electrons of 0.76 per unit cell: $\mu = -355.5\text{ meV}$, -347.5 meV , and -345.7 meV for $T = 20\text{ K}$, 100 K , and 200 K , respectively. The values of the other input parameters for the normal state are the same as those for the superconducting state given in Table 1, except for $\Delta_0 = 0$, $\Gamma = 70\text{ meV}$ (the mode is assumed to be overdamped), and $\xi = 6\text{ \AA}$. Both for the superconducting and for the normal state

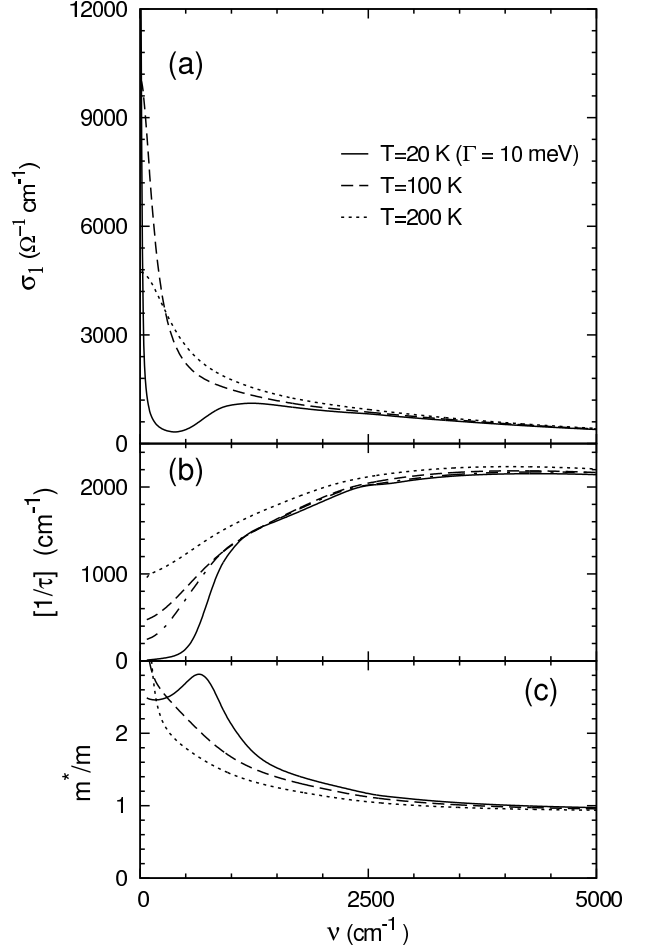


FIG. 16: Calculated temperature dependencies of the conductivity, the scattering rate, and the mass enhancement factor. The dashed-dotted line in part (b) corresponds to an unrealistic case of the normal state, $T = 100\text{ K}$, and the spin susceptibility containing the sharp mode.

we further include the continuum contribution to χ in the form introduced in Subsect. IV E, with four times larger spectral weight than that of the mode ($b_C/b_M = 4$). The 20 K and 100 K spectra of χ'' are shown in Fig. 13 (b). The calculated values of ω_{pl} and $\omega_{\text{pl,sc}}$ are 17500 cm^{-1} and 10500 cm^{-1} , respectively.

It can be seen that the model is capable of reproducing not only the main characteristics of the low temperature infrared spectra but also, at least qualitatively, the differences between the normal and the superconducting state. Our discussion will be limited to the following issues:

(i) *The frequency dependence of $\Delta\sigma_1 = \sigma_1(100\text{ K}) - \sigma_1(20\text{ K})$ in mid-infrared.* In both the experimental (see, e.g., Ref. 29) and the computed spectra (see Fig. 16), $\Delta\sigma_1$ is a positive and (approximately) decreasing function of frequency. In the experimental spectra the decrease is very rapid below $\sim 1000\text{ cm}^{-1}$, i.e., in the region of the spectral gap. Above 1000 cm^{-1} , the superconducting and the normal state spectra are close to each other and $\Delta\sigma_1$ is very small. In the computed spectra, on the other

hand, the decrease of $\Delta\sigma_1$ is relatively gradual. The discrepancy is very probably due to the fact that our approach is not self-consistent. We believe that it would vanish or diminish if a selfconsistent version of Eq. 13 (i.e., G_0 replaced with G) was used.

(ii) *The onset of $1/\tau$.* The 100 K spectrum does not display the sharp onset around 700 cm^{-1} discussed above. Nevertheless, at low frequencies it deviates slightly from the straight line that can be used to approximate $[1/\tau](\omega)$ in the region between ca 1000 cm^{-1} and 2500 cm^{-1} , an effect similar to the one of some experimental spectra^{25,26,29,54}. Obviously, this kind of deviation does not simply imply the presence of a sharp mode. For comparison we also show in Fig. 16 (b) the spectrum corresponding to an unrealistic case of the normal state, $T = 100 \text{ K}$, and the spin susceptibility containing the sharp mode ($\Gamma = 10 \text{ meV}$, $\xi = 9 \text{ \AA}$). Here the onset feature is more pronounced.

(iii) *The fine structure around 2500 cm^{-1} .* It is sharper in the superconducting state than in the normal state. This seems not to apply to the similar structure of the experimental scattering rate spectra.

(iv) *The onset of the plateau of the scattering rate spectra.* With increasing temperature, it shifts towards lower frequencies. This is consistent with the experimental data of Ref. 27.

(v) *The normal-state m^*/m spectra — low-frequency asymptotics.* Below $\sim 300 \text{ cm}^{-1}$, m^*/m rapidly increases with decreasing frequency. This is an artefact of our computational approach which has an interesting physical background. We calculate $\sigma_2(\omega)$ systematically using Eq. 26 and $\langle K \rangle$ by taking the average of the expression on the right hand side of Eq. 22. The value of $\langle K \rangle$ is very slightly (by about 2%) larger than the one given by the sum rule of Eq. 27. As a consequence, $\sigma(\omega)$ contains a small unphysical singular part, which is responsible for the behaviour of m^*/m at low frequencies. We have checked that the problem is not due to a limited precision of our numerical calculations. Instead, it seems to be caused by the neglect of vertex corrections in Eq. 29. The latter have been recently suggested to influence the response functions dramatically^{61,62}. For the present values of the parameters, their role, at least as the integrated spectral weight is concerned, appears to be only minor. They can be expected, however, to become more pronounced for higher values of g . Indeed, we have found, that the discrepancy between the results of Eqs. 22 and Eq. 27 mentioned above increases considerably with increasing g . Note finally that for $\omega > 500 \text{ cm}^{-1}$ the spectra of m^*/m are almost unaffected by the spurious component of σ .

(vi) *High-frequency asymptotics of m^*/m .* At higher frequencies, $[m^*/m](\omega, T = 20 \text{ K}) > [m^*/m](\omega, T = 100 \text{ K})$. For the present values of the parameters, the two spectra converge only slowly to their common limit of 1. At $\omega = 5000 \text{ cm}^{-1}$, the magnitude of the difference is still approximately 0.02.

2. Temperature dependence of the total intraband spectral weight

The changes of the total intraband spectral weight, $I_O = \int_0^\infty d\omega \sigma_1(\omega)$, are of particular interest, because this quantity is approximately proportional to the effective kinetic energy of the charged quasiparticles. The latter is defined by

$$\text{K.E.} = \sum_{\mathbf{k}} \varepsilon_{\mathbf{k}} n_{\mathbf{k}}, \quad n_{\mathbf{k}} = \sum_{\alpha} \langle c_{\mathbf{k}\alpha}^+ c_{\mathbf{k}\alpha} \rangle \quad (52)$$

with an obvious extension to multilayer compounds. In the case of the nearest-neighbor tight-binding dispersion relation, the sum rule of Eq. 27 reduces to

$$I_O = -\frac{\pi}{2} \frac{e^2}{d\hbar^2} \frac{1}{2} \times \text{K.E./unit cell}. \quad (53)$$

For very small values — relative to that of t — of further-neighbor hopping parameters, Eq. 53 can be expected to hold approximately. The values of the latter parameters characteristic of the real high- T_c materials are smaller yet comparable with t . It is thus not immediately clear, to what extent Eq. 53 applies. In order to obtain an insight, we first concentrate on the trivial case of noninteracting quasiparticles ($g = 0$). In the remaining part of this subsubsection we shall discuss the TD of I_O and related quantities, resulting from the spin-fermion model used above.

Figure 17 shows the computed temperature dependences of μ , K.E./unit cell, and I_O for the dispersion relation of Eq. 32 and of Ref. 20. It can be seen that (i) The chemical potential increases monotonically with increasing temperature. (ii) The kinetic energy increases with increasing temperature, approximately following a parabola. (iii) In part (a), I_O is approximately equal to one half of $-2d\hbar^2/(\pi e^2)\text{K.E.}$, in agreement with Eq. 53, and the TD of I_O also tracks the one of K.E. In part (b), the TD is more complex: I_O is approximately T -independent for $T < 200 \text{ K}$ and it decreases at higher temperatures. Note that the only generic trend is that of the point (ii). The other aspects depend very much on details of the dispersion relation. Even for the simple $t-t'$ dispersion — with the present values of the hopping parameters — both μ and I_O can either increase/decrease or decrease/increase depending on the location of the Fermi surface with respect to the Van-Hove singularity associated with the X -point. The first (second) variant occurs for the Fermi surface above (below) the singularity. Next we discuss changes of the three quantities when going from the normal to the superconducting state. (i) The chemical potential increases in both cases. This can be explained as follows: in the superconducting state the region of the BZ around the Van-Hove singularity becomes partially unoccupied and the chemical potential has to increase in order that the particle number would be conserved. (ii) The kinetic energy increases, a characteristic feature of the BCS theory. (iii) In part (a) the

spectral weight I_O behaves similarly as $-\text{K.E.}$, in agreement with Eq. 53. In part (b), however, I_O very slightly increases, contrary to what one would expect based on Eq. 53. Again, only the trend of the point (ii) is a generic one.

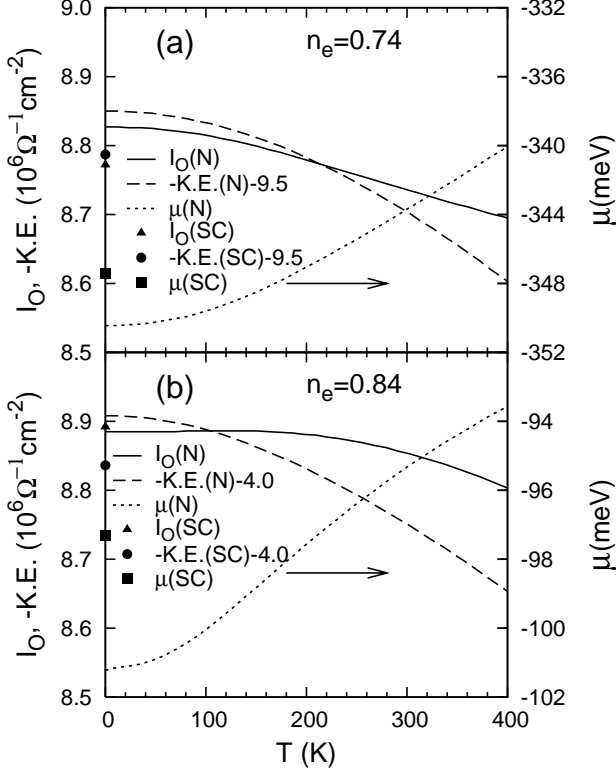


FIG. 17: Temperature dependencies of the total intraband spectral weight I_O , the effective kinetic energy per unit cell multiplied by $-2d\hbar^2/(\pi e^2)$ (labelled as $-\text{K.E.}$), and the chemical potential for noninteracting quasiparticles. Parts (a) and (b) correspond to the dispersion relations of Eq. 32 and of Ref. 20, respectively. For each temperature, the value of the chemical potential was adjusted to yield the total number of electrons per unit cell of 0.74 (a) and 0.84 (b). The symbols correspond to the BCS ansatz with the superconducting gap given by Eq. 33.

Figure 18 shows the computed temperature dependencies of μ , $\text{K.E.}/\text{unit cell}$, and I_O for quasiparticles coupled to the spin fluctuations. The dispersion relation of Eq. 32 and the model spin susceptibility introduced in the preceding subsection and subsubsection have been used. The normal-state trends are similar to those of Fig. 17 (a): μ and K.E. increase and I_O decreases. Both the quantities K.E. , I_O , and their changes, $\Delta I_O = I_O(200 \text{ K}) - I_O(20 \text{ K})$ and $\Delta \text{K.E.} = \text{K.E.}(200 \text{ K}) - \text{K.E.}(20 \text{ K})$, approximately fulfill Eq. 53. The changes occurring upon entering the superconducting state (at $T = 20 \text{ K}$) are the following: μ decreases by $\sim 5 \text{ meV}$, K.E. increases, and I_O decreases. The magnitudes of the changes of K.E. and I_O are surprisingly similar to those of Fig. 17, $\Delta I_O = I_O(\text{SC}, T = 20 \text{ K}) - I_O(\text{N}, T = 20 \text{ K}) = -0.04 \cdot 10^6 \Omega^{-1} \text{cm}^{-2}$. Next

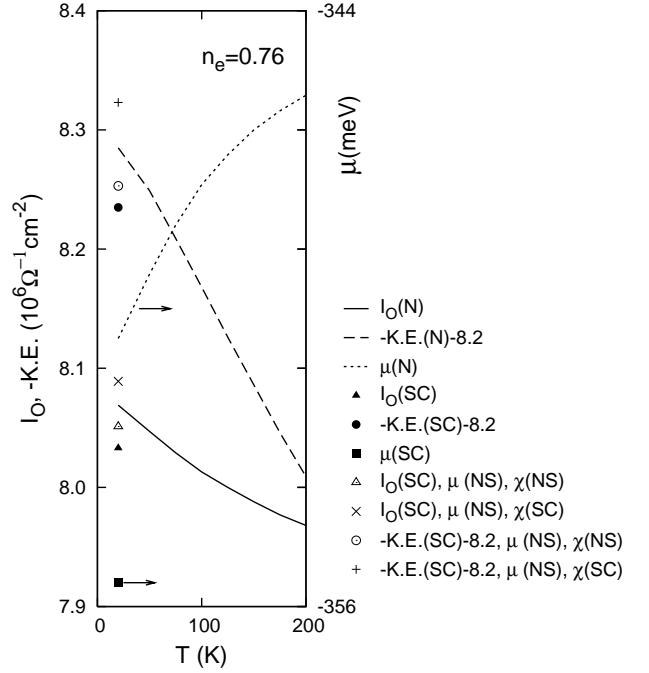


FIG. 18: The same as in Fig. 17 but for quasiparticles coupled to the spin fluctuations. The lines correspond to the normal state and the solid symbols to the superconducting state. For each value of T the value of μ was adjusted to yield the total number of electrons per unit cell of 0.76. The open symbols (the symbol \times and the star) correspond to an unrealistic case of the superconducting state, $\mu = \mu(\text{normal state}, T = 20 \text{ K})$, $\chi(\mathbf{q}, \omega) = \chi(\text{normal state}, T = 20 \text{ K}, \mathbf{q}, \omega)$ [$\chi(\mathbf{q}, \omega) = \chi(\text{superconducting state}, T = 20 \text{ K}, \mathbf{q}, \omega)$].

we propose an interpretation of these effects associated with the superconducting transition. For the present purposes and within the context of our approach the latter transition can be thought of as consisting of three stages: (i) Opening of the superconducting gap without relaxing the chemical potential and the spin susceptibility. (ii) “Improving” (sharpening) of the quasiparticles due to the superconductivity related change of the spin susceptibility, in particular, due to the formation of the spin gap (which is, within our naive model, achieved by the narrowing of the low frequency component of χ), still without relaxing μ . This is the feedback effect of the spin fluctuations on the quasiparticles which has been already considered by several authors^{63,64,65}. (iii) Change of the momentum distribution function $n_{\mathbf{k}}$ connected with the change of μ which is reinforced by the requirement of particle-number conservation. The first stage results in an increase of K.E. and a related decrease of I_O , see the open symbols in Fig. 18. These are the same effects as in Fig. 17 (a) and their explanation is trivial. The second stage is associated with a decrease of K.E. and an increase of I_O , see the symbols $+$ and \times in Fig. 18. These effects are basically due to the fact that the superconducting state is, as regards the momentum distribution function, more Fermi-liquid like than the normal state^{64,65}. If it

were only for the two stages, (i) and (ii), the K.E. (I_O) would—for the present values of the input parameters—decrease (increase) when going from the normal to the superconducting state. The third stage, however, can reverse the result. This is what happens for the present values of the input parameters. A lesson one can learn from the example of this subsubsection is that the changes of K.E. and I_O associated with the superconducting transition are determined by a delicate competition of the three ingredients: the opening of the superconducting gap, the feedback effect of the spin fluctuations on the quasiparticles, and the chemical potential shift, which may be large because of an inherent electron-hole asymmetry. So far we have considered changes occurring at a fixed temperature of 20 K. These are not directly accessible to experimental investigations and can only be obtained by a careful elimination of the normal state trend. The quantity $\Delta'I_O = I_O(\text{SC}, T = 20 \text{ K}) - I_O(\text{N}, T = 100 \text{ K})$, however, can be measured. Our calculations yield a small and positive value of $\Delta'I_O$ of $0.015 \cdot 10^6 \Omega^{-1} \text{cm}^{-2}$.

V. SUMMARY AND CONCLUSIONS

In Subsects. IV A-IV D we have analyzed the structures of the superconducting state (SCS) conductivity reflecting the coupling of the charge quasiparticles to the resonance mode: the onset of the real part $\sigma_1(\omega)$ of the conductivity starting around the frequency ω_0 of the mode and the maximum of the function $W(\omega)$ centered approximately at $\omega = \omega_0 + \Delta_0/\hbar$, where Δ_0 is the maximum value of the superconducting gap. Our analysis provides a clear interpretation of both features. It is based on a division of the Brillouin into three parts: the nodal, the region, and the intermediate. Both $\sigma_1(\omega)$ and $W(\omega)$ can be expressed as the sums of contributions of the three parts, whose structures can be easily related to those of the quasiparticle spectral function $A(\mathbf{k}, \omega)$. This gives us a possibility to understand also the features of $\sigma_1(\omega)$ and $W(\omega)$ in terms of $A(\mathbf{k}, \omega)$. We have shown that the onset is due to the appearance above ω_0 of low energy excitations of the nodal region, consisting of two nodal quasiparticles and the mode. For the conventional shape of the d -gap the onset is very gradual but it becomes steeper with increasing broadening of the nodes. The maximum of $W(\omega)$ has been shown to be due to the appearance above $\omega_{CSB} = \omega_0 + \Delta_0/\hbar$ of excitations of the nodal region, consisting of a nodal particle, an antinodal particle and the mode. Due to the Brillouin zone averaging, in particular, due a considerable contribution of the intermediate region, the maximum of $W(\omega)$ appears at a frequency Ω_M which is slightly higher but considerably lower than $\omega_0 + (2\Delta_0/\hbar)$. This result of our analysis confirms, to some extent, the claim by Carbotte, Schachinger, and Basov, that the frequency of the maximum is approximately equal to Ω_{CSB} . The width of the maximum, however, is determined not only by the one of the mode but also by the averaging. For zero width of

the mode, the FWHM of the maximum is ca 160 cm^{-1} .

In the light of the present analysis, the interpretation of the onset feature in the SCS infrared spectra in terms of the neutron resonance remains to be very plausible. In fact, we are not aware of any other comparable explanation. An encouraging finding is that the values of the coupling constant to be used in conjunction with the properly normalized spin susceptibility are of the same order of magnitude as those of U expected to be relevant for the HTCS.

In Subsect. IV E we have studied the role of the spin-fluctuation continuum. The computed spectra of the scattering rate $1/\tau$ exhibit a sharp step (onset feature) centered around Ω_M , a region of an approximately linear increase of $1/\tau$, and a plateau in the mid-infrared. The height of the step is determined by the spectral weight I_R of the mode, the difference between the value of $1/\tau$ of the plateau and the height of the step by the spectral weight I_C of the continuum, and the onset frequency of the plateau by the width of the continuum. The experimental scattering rate spectra can be reproduced using values of I_C/I_M of 5-10 and those of the width of several hundreds meV. The computed spectra of $1/\tau$ display, in addition, an interesting weak structure located approximately at $\mu - \epsilon_\Gamma + \Delta_0 + \hbar\omega_0$ (μ is the chemical potential and ϵ_Γ the quasiparticle energy of the Γ -point). The presence of this structure in the experimental spectra would allow one to estimate the width of the occupied part of the band.

Finally, in Subsect. IV F we have concentrated on the temperature dependence of the spectra. The main differences between the SCS and the normal state (NS) experimental data, in particular, the spectral gap, the tail of $\sigma_1(\omega, \text{NS}) - \sigma_1(\omega, \text{SCS})$ ranging to very high frequencies, and the shift of the scattering rate plateau towards lower frequencies with increasing temperature are reasonably well reproduced. Some of the remaining discrepancies are very likely to be related to the absence of self-consistency and vertex corrections. We have further investigated the temperature dependence of the effective kinetic energy K.E. and of the intraband spectral weight I_O , first for the BCS case and second for the present version of spin-fermion model. In the BCS case, K.E. increases both with increasing temperature in the NS and when going from the NS to the SCS. The spectral weight behaves similarly as $-K.E.$ only for the simpler of the two (realistic) dispersion relations used (the “ $t - t'$ ” dispersion relation) and for the Fermi surface above the Van-Hove singularity. For the other dispersion relation even the sign of the change of I_O between the NS and the SCS differs from the one of $-K.E.$. The estimates of the (in-plane) kinetic energy changes based on optical data should thus be taken with caution. The temperature dependencies of K.E. and I_O calculated for the case of the quasiparticles coupled to the spin fluctuations are, for the present values of the input parameters, similar to those of the BCS, $t - t'$ case. The physics underlying the differences between the NS and the SCS, however, is more complicated. It involves

three different mechanisms causing changes of the occupation numbers $n_{\mathbf{k}}$: the opening of the gap [leading to an increase (decrease) of K.E. (I_O)], a sharpening of the quasiparticles in the SCS associated with the formation of the spin gap (resulting in an opposite trend), and a chemical potential shift (leading here to the same trend as the opening of the gap). While the mechanisms are certainly generic, the outcome of their competition, may depend on details.

Acknowledgments

This work was supported by the Ministry of Education of CR (MSM0021622410). D. M. thanks the AvH foundation for support during a short stay at MPI Stuttgart. Discussions with A. Dubroka, A. V. Boris, N. N. Kovaleva, and B. Keimer are gratefully acknowledged.

* Electronic address: munzar@physics.muni.cz

- ¹ M. R. Norman and C. Pepin, Rep. Prog. Phys. **66**, 1547 (2003).
- ² A. Abanov, A. V. Chubukov, and J. Schmalian, Adv in Phys. **52**, 119 (2003).
- ³ N. E. Bickers and D. J. Scalapino, Ann. Phys. (N. Y.) **193**, 206 (1989).
- ⁴ P. Monthoux and D. J. Scalapino, Phys. Rev. Lett. **72**, 1874 (1994).
- ⁵ C.-H. Pao and N. E. Bickers, Phys. Rev. Lett. **1870**, 72 (1994).
- ⁶ T. Dahm and L. Tewordt, Phys. Rev. Lett. **74**, 793 (1995).
- ⁷ D. J. Scalapino, Phys. Rep. **250**, 329 (1995).
- ⁸ A. I. Lichtenstein, O. Gunnarson, O. K. Andersen, and R. M. Martin, Phys. Rev. B **54**, 12505 (1996).
- ⁹ D. Manske, I. Eremin, and K. H. Bennemann, Phys. Rev. Lett. **87**, 177005 (2001).
- ¹⁰ A. K. McMahan, R. M. Martin, and S. Satpathy, Phys. Rev. B **38**, 6650 (1988).
- ¹¹ M. S. Hybertsen, M. Schlüter, and N. E. Christensen, Phys. Rev. B **39**, 9028 (1989).
- ¹² P. Monthoux, A. V. Balatsky, and D. Pines, Phys. Rev. B **46**, 14803 (1992).
- ¹³ P. Monthoux and D. Pines, Phys. Rev. B **47**, 6069 (1993).
- ¹⁴ P. Monthoux and D. Pines, Phys. Rev. B **49**, 4261 (1994).
- ¹⁵ A. J. Millis, H. Monien, and D. Pines, Phys. Rev. B **42**, 167 (1990).
- ¹⁶ H. F. Fong, B. Keimer, D. Reznik, D. L. Milius, and I. A. Aksay, Phys. Rev. B **54**, 6708 (1996).
- ¹⁷ H. F. Fong, P. Bourges, Y. Sidis, L. P. Regnault, A. Ivanov, G. D. Gu, N. Koshizuka, and B. Keimer, Nature **398**, 588 (1999).
- ¹⁸ H. F. Fong, P. Bourges, Y. Sidis, L. P. Regnault, J. Bossy, A. Ivanov, D. L. Milius, I. A. Aksay, and B. Keimer, Phys. Rev. B **61**, 14773 (2000).
- ¹⁹ H. He, P. Bourges, Y. Sidis, C. Ulrich, L. P. Regnault, S. Pailhès, N. S. Berzigarova, N. N. Kolesnikov, and B. Keimer, Science **295**, 1045 (2002).
- ²⁰ M. Eschrig and M. Norman, Phys. Rev. B **67**, 144503 (2003).
- ²¹ A. Damascelli, Z. Hussain, and Z.-X. Shen, Rev. Mod. Phys. **75**, 473 (2003).
- ²² E. Schachinger, J. P. Carbotte, and F. Marsiglio, Phys. Rev. B **56**, 2738 (1997).
- ²³ S. M. Quinlan, P. J. Hirschfeld, and D. J. Scalapino, Phys. Rev. B **53**, 8575 (1996).
- ²⁴ A. V. Puchkov, D. N. Basov, and T. Timusk, J. Phys. Condens. Matter **8**, 10049 (1996).
- ²⁵ C. Bernhard, T. Holden, J. Humlíček, D. Munzar, A. Golnik, M. Klášer, T. Wolf, L. Carr, C. Holmes, B. Keimer, et al., Solid State Commun. **121**, 93 (2002).
- ²⁶ J. J. Tu, C. C. Homes, G. D. Gu, D. N. Basov, and M. Strongin, Phys. Rev. B **66**, 144514 (2002).
- ²⁷ D. van der Marel, H. J. A. Molegraaf, J. Zaanen, Z. Nussinov, F. Carbone, A. Damascelli, H. Eisaki, M. Greven, P. H. Kes, and M. Li, Nature **425**, 271 (2003).
- ²⁸ C. C. Homes, S. V. Dordevic, D. A. Bonn, R. Liang, and W. N. Hardy, Phys. Rev. B **69**, 024514 (2004).
- ²⁹ A. V. Boris, N. N. Kovaleva, O. V. Dolgov, C. T. Lin, B. Keimer, and C. Bernhard, Science **121**, 93 (2004).
- ³⁰ D. Munzar, C. Bernhard, and M. Cardona, Physica C **312**, 121 (1999).
- ³¹ J. P. Carbotte, E. Schachinger, and D. N. Basov, Nature **401**, 354 (1999).
- ³² The relation can be easily obtained using the formalism summarized in the lecture notes of S. V. Schulga: S. V. Schulga, in *Material Science, Fundamental Properties and Future Electronic Applications of High-Tc Superconductors*, edited by S. L. Drechsler and T. Mischonov (Kluwer Academic, Dordrecht, 2001), pp. 323-360; also published as cond-mat/0101243.
- ³³ A. Abanov, A. V. Chubukov, and J. Schmalian, Phys. Rev. B **63**, 180510 (2001).
- ³⁴ A. Abanov, A. V. Chubukov, and J. Schmalian, J. Electron Spectrosc. **117**, 129 (2001).
- ³⁵ J. R. Schrieffer, *Theory of Superconductivity* (Addison-Wesley, Reading, 1988).
- ³⁶ A. W. Sandvik, D. J. Scalapino, and N. E. Bickers, Phys. Rev. B **69**, 094523 (2004).
- ³⁷ E. Schachinger, J. J. Tu, and J. P. Carbotte, Phys. Rev. B **67**, 214508 (2003).
- ³⁸ H. J. A. Molegraaf, C. Presura, D. V. der Marel, P. H. Kes, and M. Li, Science **295**, 2239 (2002).
- ³⁹ G. D. Mahan, *Many Particle Physics* (Kluwer Academic/Plenum Publishers, New York, 2000), Chapt. 3.8.
- ⁴⁰ D. J. Scalapino, S. R. White, and S. C. Zhang, Phys. Rev. Lett. **68**, 2830 (1992).
- ⁴¹ For a derivation of the formula see Chapt. 8 of Ref. ³⁵.
- ⁴² Eq. ³¹ has been derived along the lines of Chapt. 8.1.2 of Ref. ³⁹.
- ⁴³ O. K. Andersen, A. I. Lichtenstein, O. Jepsen, and F. Paulsen, J. Phys. Chem. Solids **56**, 1573 (1995).
- ⁴⁴ D. L. Feng, N. D. Armitage, D. H. Lu, A. Damascelli, J. P. Hu, P. Bogdanov, A. Lanzara, F. Ronning, K. M. Shen, H. Eisaki, et al., Phys. Rev. Lett. **86**, 5550 (2001).
- ⁴⁵ Y. D. Chuang, A. D. Gromko, A. Fedorov, Y. Aiura, K. Oka, Y. Ando, H. Eisaki, S. I. Uchida, and D. S. Dessau, Phys. Rev. Lett. **87**, 117002 (2001).
- ⁴⁶ A. A. Kordyuk, S. V. Borisenko, T. K. Kim, K. A. Nenkov, M. Knupfer, J. Fink, M. S. Golden, H. Berger, and R. Fol-

lath, Phys. Rev. Lett. **89**, 077003 (2002).

⁴⁷ M. Eschrig and M. R. Norman, Phys. Rev. Lett. **89**, 277005 (2002).

⁴⁸ S. V. Borisenko, A. A. Kordyuk, T. K. Kim, A. Koitzsch, M. Knupfer, J. Fink, M. S. Golden, M. Eschrig, H. Berger, and R. Follath, Phys. Rev. Lett. **90**, 207001 (2003).

⁴⁹ Jian-Xin Li, T. Zhou, and Z. D. Wang, cond-mat/0501356 (unpublished).

⁵⁰ S. Pailhes, Y. Sidis, P. Bourges, C. Ulrich, V. Hinkov, L. P. Regnault, A. Ivanov, B. Liang, C. T. Lin, C. Bernhard, et al., Phys. Rev. Lett. **91**, 237002 (2003).

⁵¹ H. Y. Kee, S. A. Kivelson, and G. Aeppli, Phys. Rev. Lett. **88**, 257002 (2002).

⁵² A. Abanov, A. V. Chubukov, M. Eschrig, M. R. Norman, and J. Schmalian, Phys. Rev. Lett. **89**, 177002 (2002).

⁵³ Note that the authors of Ref. 20 use the spin susceptibility normalized to the experimental value of the spectral weight of the mode. Furthermore, their formula for the selfenergy does not contain the factor of 3/4 of Eq. 13. The effective value of g corresponding to their spin susceptibility normalized according to Eq. 35 and our selfenergy formula is about 0.25 eV.

⁵⁴ J. Hwang, T. Timusk, and G. D. Gu, Nature **295**, 1045 (2004).

⁵⁵ E. Schachinger and J. P. Carbotte, Phys. Rev. B **62**, 9054 (2000).

⁵⁶ E. J. Singley, D. N. Basov, K. Kurahashi, T. Uefuji, and K. Yamada, Phys. Rev. B **64**, 224503 (2001).

⁵⁷ N. L. Wang, P. Zheng, J. L. Luo, Z. J. Chen, S. L. Yan, L. Fang, and Y. C. Ma, Phys. Rev. B **68**, 054516 (2003).

⁵⁸ S. V. Dordevic and C. C. Homes and J. J. Tu and T. Valla and M. Strongin and P. D. Johnson and G. D. Gu and D. N. Basov, cond-mat/0411043 (unpublished).

⁵⁹ In order to obtain the scattering rate spectra from optical data one has to make an assumption regarding the interband contribution to the dielectric function. This brings about a certain degree of arbitrariness.

⁶⁰ Z. X. Shen, W. E. Spicer, D. M. King, D. S. Dessau, and B. O. Wells, Science **267**, 343 (1995).

⁶¹ A. J. Millis and H. D. Drew, Phys. Rev. B **67**, 214517 (2003).

⁶² A. J. Millis, A. Zimmers, R. P. S. M. Lobo, and N. Bonnemps, cond-mat/0411172 (unpublished).

⁶³ M. R. Norman, M. Randeira, B. Janko, and J. C. Campuzano, Phys. Rev. B **61**, 14742 (2000).

⁶⁴ M. R. Norman and C. Pépin, Phys. Rev. B **66**, 100506 (2002).

⁶⁵ Y. Yanase and M. Ogata, cond-mat/0412508 (unpublished).